Environmental Research 252 (2024) 119046

Contents lists available at ScienceDirect

Environmental Research

journal homepage: www.elsevier.com/locate/envres

Zinc oxide decorated plantain peel activated carbon for adsorption of cationic malachite green dye: Mechanistic, kinetics and thermodynamics modeling

Adewumi Oluwasogo Dada [a,b,c,d,e,*], Abosede Adejumoke Inyinbor [a,c,e], Blessing Enyojo Tokula [a,c,e,**], Abiodun Ajibola Bayode [f], Kehinde Shola Obayomi [g,h], Christiana Oluwatoyin Ajanaku [a,c], Folahan Amoo Adekola [i], Kolawole Oluseyi Ajanaku [a], Ujjwal Pal [b,***]

[a] Industrial Chemistry Programme, Nanotechnology Laboratory, Department of Physical Sciences, Landmark University, P.M.B.1001, Omu-Aran, Kwara, Nigeria
[b] Department of Energy & Environmental Engineering, CSIR-Indian Institute of Chemical Technology, Hyderabad, 500007, India
[c] Landmark University Sustainable Development Goal 6: Clean Water and Sanitation, P.M.B.1001, Omu-Aran, Kwara, Nigeria
[d] Landmark University Sustainable Development Goal 7: Affordable and Clean Energy, P.M.B.1001, Omu-Aran, Kwara, Nigeria
[e] Landmark University Sustainable Development Goal 11: Sustainable Cities and Communities, P.M.B.1001, Omu-Aran, Kwara, Nigeria
[f] Department of Chemical Sciences, Redeemer's University, P.M.B 230, Ede, Osun State, Nigeria
[g] Department of Chemical Engineering, Curtin University, CDT 250, 98009, Miri, Sarawak, Malaysia
[h] Institute for Sustainable Industries and Liveable Cities, Victoria University, Werribee, VIC, 3030, Australia
[i] Department of Industrial Chemistry, University of Ilorin, P.M.B. 1515, Ilorin, Kwara State, Nigeria

ARTICLE INFO

Keywords:
ZnO-Doped-PPAC nanocomposites
Malachite green
Endocrine disrupting chemicals
Isotherm
Kinetics and thermodynamics

ABSTRACT

Reports have shown that malachite green (MG) dye causes various hormonal disruptions and health hazards, hence, its removal from water has become a top priority. In this work, zinc oxide decorated plantain peels activated carbon (ZnO@PPAC) was developed via a hydrothermal approach. Physicochemical characterization of the ZnO@PPAC nanocomposite with a 205.2 m^2/g surface area, porosity of 614.68 and dominance of acidic sites from Boehm study established the potency of ZnO@PPAC. Spectroscopic characterization of ZnO@PPAC vis-a-viz thermal gravimetric analyses (TGA), Fourier Transform Infrared Spectroscopy (FTIR), Powdered X-ray Diffraction (PXRD), Scanning Electron Microscopy and High Resolution – Transmission Electron Microscopy (HR-TEM) depict the thermal stability via phase transition, functional group, crystallinity with interspatial spacing, morphology and spherical and nano-rod-like shape of the ZnO@PPAC heterostructure with electron mapping respectively. Adsorption of malachite green dye onto ZnO@PPAC nanocomposite was influenced by different operational parameters. Equilibrium data across the three temperatures (303, 313, and 323 K) were most favorably described by Freundlich indicating the ZnO@PPAC heterogeneous nature. 77.517 mg/g monolayer capacity of ZnO@PPAC was superior to other adsorbents compared. Pore-diffusion predominated in the mechanism and kinetic data best fit the pseudo-second-order. Thermodynamics studies showed the feasible, endothermic, and spontaneous nature of the sequestration. The ZnO@PPAC was therefore shown to be a sustainable and efficient material for MG dye uptake and hereby endorsed for the treatment of industrial effluent.

* Corresponding author. Industrial Chemistry Programme, Nanotechnology Laboratory, Department of Physical Sciences, Landmark University, P.M.B.1001, Omu-Aran, Kwara, Nigeria.
** Corresponding author. Industrial Chemistry Programme, Nanotechnology Laboratory, Department of Physical Sciences, Landmark University, P.M.B.1001, Omu-Aran, Kwara, Nigeria.
*** Corresponding author. Department of Energy & Environmental Engineering, CSIR-Indian Institute of Chemical Technology, Hyderabad-500007, India.
E-mail addresses: dada.oluwasogo@lmu.edu.ng (A.O. Dada), tokula.blessing@lmu.edu.ng (B.E. Tokula), ujjwalpal@iict.resin (U. Pal).

https://doi.org/10.1016/j.envres.2024.119046
Received 10 February 2024; Received in revised form 19 March 2024; Accepted 28 April 2024
Available online 3 May 2024

1. Introduction

Dyes are highly hazardous to human health on account of their carcinogenic and mutagenic properties. Their complex structures and synthetic origin make them inert, not easily biodegraded and highly toxic (Bayode et al., 2020a; Thi et al., 2023). Most industries use dyes for most of their products, the yearly consumption is about 10,000 tons and disposal has become a challenge (Mosebolatan et al., 2023). Over 10–15 % are indiscriminately introduced into water bodies which have undesirable effects on aquatic life and humans (Abewaa et al., 2023). Malachite green (MG) dyes are part of the major dyes in the triphenylmethane family(Somsiripan and Sangwichien, 2023). MG dyes are organic, water-soluble, and cationic. MG finds application in several industries such as the jute and silk industry, aquaculture and fisheries as ectoparasites and fungicides, and textile industries for colouring wool, cotton, paper, acrylic fibres and leather (Liu et al., 2020), (Cui et al., 2023). The extensive use of MG dye has led to its entrance into the food chain which causes harm to humans and animals through direct contact, inhalation, or ingestion due to its mutagenic, carcinogenic, and teratogenic properties (Elwardany et al., 2023), (Hock et al., 2023). MG dye has been highlighted as one of the causes of palpitations (Bai et al., 2022), headaches (Obayomi et al., 2023a), eye irritations (Obayomi et al., 2023b), several skin diseases and hormonal disruptions (Giri et al., 2022). Similarly, the breakdown products of MG can also be toxic and carcinogenic and the decontamination of MG from water is a great challenge owing to its complex chemical structure(Merrad et al., 2023), (Taha, 2023). Therefore, MG must be eliminated from industrial effluents before their disposal in aquatic environments.

Several conventional approaches and technical routes have been reported for the sequestration of dyes (Abewaa et al., 2023). Most of these methods suffer some weaknesses which eventually place adsorption as a preferred and cost-effective technique. Various studies have established the efficacy of the adsorption technique for the uptake of different pollutants (Hock et al., 2023; Taha, 2023; Dada et al., 2023). The sorption technique is generally known for its simple operation (Li et al., 2023), minimal initial cost (Guo et al., 2023) and excellent removal performance. Amongst the several applicable sorbents like clay (Taha, 2023), chitosan (Wang et al., 2024a), (Muinde et al., 2020), and activated alumina (Kuang et al., 2018), (Y et al., 2022), there have been reports on the use of activated carbon as an adsorbent as being highly efficient and is preferred by dint of their large surface area (Feng et al., 2024), multiple sites for adsorption, ease of modification, high porosity and functional groups (Obayomi et al., 2023a, 2023b). Because the cost of the precursor for commercially sold activated carbon is high, therefore is a need to identify more cost-effective alternatives form indigenous and readily available material.

Wastes from agricultural sources have been identified and reported as cheap and efficient alternatives that could be applied as sustainable adsorbents effective for decontamination of wastewater (Giri et al., 2022; Merrad et al., 2023) ranging from removal of heavy metals (Taha, 2023; Dada et al., 2023), dyes (Thi et al., 2023; Li et al., 2023) and phenols (Hemmati et al., 2016), (Anna et al., 2018). Various techniques to boost the porosity, pore volume and surface area of agricultural wastes have been previously reported (Alipanahpour Dil et al., 2019), (Firdaus et al., 2023). This is carried out via surface modification either through carbonization (physical activation) or through treatment with acids, bases and salts (chemical activation) (Adegoke and Bello, 2015).

The conversion and application of plantain peel for wastewater treatment are identified as a technique for waste-to-wealth conversion. The adsorptive removal of lead (II) heavy metal was investigated by (Sudhakar et al., 2015) using unripe plantain peels. The uptake was discovered as being endothermic, favourable, and feasible. In a similar study, the uptake of Chromium present in battery recycling effluent using plantain wastes was studied by Adeolu et al. (2016) and the report established that the activated carbon obtained in the treatment of plantain peel had the highest sorption capacity. Similar outcomes were obtained by Adekola et al. (2019) who explored the potency of plantain peel-activated biochar to remediate Rhodamine B (RhB) dye-contaminated media. RhB dye removal efficiency of 54.78% was observed with an 84.41 mg/g maximum adsorption for 120 min.

Furthermore, adsorbents with higher adsorption capacity can be derived by the preparation of nanocomposites (Zheng et al., 2020), (Shayesteh et al., 2016). The loading of nanoparticles onto the activated carbon to form nanocomposites incorporates and creates unique features in the adsorbent such as greater pore size and volume, as well as a higher surface area (Xu et al., 2023). The nanocomposites have been reported to have high reusability and regeneration capacity and can be utilized severally without a decrease in their adsorption effectiveness (Masoudian et al., 2019). Due to the unavoidable use of MG dye, it is a great necessity to develop cheap methods for removing this eco-threatening contaminant. As best as we could determine, there is not report found on the adsorption of MG onto ZnO@PPAC nanocomposite majorly the purpose of embarking on this study. PPAC was adorned with ZnO to develop enhanced characteristics that would give relevance to newly developed as-synthesized ZnO@PPAC.

The objectives of this research are to explore the hydrothermal synthesis of as-synthesized ZnO-adorned-doped-PPAC, study the physicochemical and spectroscopic characterization and in application investigate the mechanistic, kinetics, isotherm and thermodynamics modelling of adsorption of endocrine disruptive malachite green. The equilibrium data obtained at three temperatures (303, 313 and 323 K) were tailored differently to four (4) isotherm models (Dubinin-Kaganer-Raduskevich, Freundlich, Temkin and Langmuir). The adsorptive capacity of ZnO@PPAC for effective adsorption of MG was quantified using various isotherm models investigated at 303, 313 and 323 K. Most studies commonly reported have always been on one temperature which may not be the best replicate of the adsorption performance of adsorbent, hence the need for adsorption of investigation at three temperatures. Mechanistic and kinetic data obtained from kinetic studies helped in determining the controlling pathway of reaction (whether it be physisorption or chemisorption) and the mechanism of MG adsorption reaction if it is diffusion-dominated. Equilibrium studies were investigated at three (3) temperatures (303, 313 and 323 K) contrary to only one temperature which is commonly and always presented by researchers. At different adsorption temperatures, the actual and absolute performances of ZnO@PPAC nanocomposites were determined. Furthermore, insight into controlling pathways and mechanisms of malachite adsorption in terms of kinetics was studied. The rate at which this endocrine disruptive dye was removed using enhanced and adorned-doped ZnO@PPAC was demonstrated by kinetic models which were determined via Intraparticle Diffusion, Pseudo-first-order, Elovich and Pseudo-second-order. Detailed assessment of the thermodynamics parameters in terms of entropy, sorption energy enthalpy, Gibb's free energy and activation energy were all assessed. The outcome of this study earned credibility and relevance to sustainable, low-cost, and environmentally friendly ZnO@PPAC. Utilization of ZnO@PPAC in excellent and effective adsorption of problematic and endocrine disruptor MG dye has successfully enlisted this as-synthesized among promising adsorbents recommended for industrial accessibility and large-scale utilization to solve waste-water pollution problems at a field scale.

2. Materials and methods

2.1. Materials

All chemicals and reagents purchased and utilized were of analytical grade. Orthophosphoric acid (H_3PO_4) (supplied by BDH chemicals CAS: 7654-37-2), Zinc Nitrate (Zn $(NO_3)_2$, (LOBA Chemie CAS: 10176-18-17), distilled water, Malachite green, Sodium hydroxide (Carlo Erba CAS: 1311-74-3), Magnetic stirrer (Bante MS300), crucibles, centrifuge (SIGMA 4–5L), desiccator, oven, sieve, (GENLAB N30C), evaporating

dish, furnace (Searchtech SX-5-12), pH meter (Hanna HI 2310), thermostat shaker model SI-300R (Lab Companion®), UV/Vis spectrophotometer model M51 (Bel Engineering®).

2.2. Plantain peel activated carbon from agro-residue

Agro-residue plantain peel obtained from the kitchen waste of Landmark University (An agro-revolutionary driven-based University in Nigeria, 8.1226° N, 5.0828° E) was screened and thoroughly washed. After washing the plantain peels were allowed to air-dry followed by oven drying for about 8 h at 105 °C. This was ground and labelled as Plantain Peel (PP) and thereafter carbonized at 400 °C for 1 h (Tokula et al., 2023a; Wang et al., 2017). The treated PP (50.0 g) was introduced into a beaker and 1 M H_3PO_4 (1000 mL) was introduced. The beaker contents were allowed to heat until evaporation of the acid took place, and a slurry was formed. This obtained slurry was heated for 1 h at 400 °C in a furnace for the activation process to be complete. The resulting activated carbon was left to cool in a desiccator and continuously washed with distilled water till a pH value of 7 was obtained. The neutral activated carbon was allowed to dry in an oven and stored in an airtight container with the label PPAC. Scheme 1 summarily described the development of this cheap, cost-effective, eco-friendly, and environmentally benign PPAC.

2.3. Zinc oxide doped PPAC (ZnO@PPAC) nanocomposite synthesis

The preparation of Zinc Oxide doped PPAC nanocomposite was carried out via a combination of bottom-up and hydrothermal techniques by improving on our earlier reported methods (Dada et al., 2023; Santhosh et al., 2021; Bayode et al., 2020b; Ahmed et al., 2017). Firstly, the ZnO nanoparticle precursor was prepared by slow addition of 1.0 M NaOH (100 mL) to 0.45 M Zinc Nitrate solution (100 mL) under constant stirring at 70 °C. The mixture was then centrifuged at 6000 rpm for 30 min and rinsed with water (distilled) and ethanol. It was then calcined for 3 h at 500 °C. The sample was then left to cool and labelled as ZnO in an airtight container.

The as-synthesized-ZnO@PPAC nanocomposite was developed typically by introducing 50% PPAC (agro-residue precursor) to a mixture of absolute ethanol (ethanolic water) which was homogenized via sonication for an hour. Next, 50% of as-prepared ZnO was introduced and further homogenized by sonication for 2 h. The mixture was placed in a Teflon-sealed hydrothermal autoclave (100 mL) for 3 h to be heated at 120 °C in an oven to develop ZnO@PPAC. This was later centrifuged (using the REMI–R–24 model) at 6000 rpm for 15 min and decanted. The developed as-synthesized-ZnO@PPAC was dried and kept air-tight for further characterization and adsorption application. The flow chart for the synthesis of ZnO@PPAC is presented in Scheme 2.

2.4. Spectroscopic characterization

The unique spectroscopic properties of as-synthesized ZnO@PPAC were investigated using a combination of TGA, FTIR, XRD, SEM and TEM state-of-the-art equipment with the model described in the ESI Section 2. The adsorbent underwent Fourier Transform Infrared Spectroscopy (FTIR) analysis to ascertain the existence of any potential functional groups that might be present (Ding et al., 2015). The X-ray Diffraction (XRD) technique however is used to examine the adsorbent's crystalline nature and mineral constituents. The thermal stability and phase were determined using Thermogravimetric analysis (TGA), derivative of thermal gravimetric (DTG), and differential scanning calorimetric (DSC). The nature of the surface characteristics and morphology of the ZnO@PPAC was determined by Scanning Electron Microscopy (SEM) examination. In this technique, the ZnO@PPAC surface was captured in three-dimensional form by detectors in the SEM (Deb et al., 2019). Shape, electron mapping and selected area electron diffraction pattern indicating the elemental constituents of as-synthesized ZnO@PPAC were assessed by HR-TEM.

2.5. Batch adsorption studies

2.5.1. MG dye solution preparation

Stock solutions of the MG dye adsorbate were made via the addition of 1.0 g of adsorbate (MG) into distilled water (1000 mL). Working standards from 10 to 50 ppm were prepared by appropriate serial dilution.

2.5.2. Batch adsorption involving various operational parameters

For the adsorption studies, an adsorbent weight of 1.0 g was placed into 100 mL of MG dye solution. The contents were then shaken at various time intervals using a mechanical shaker (Choudhary et al.,

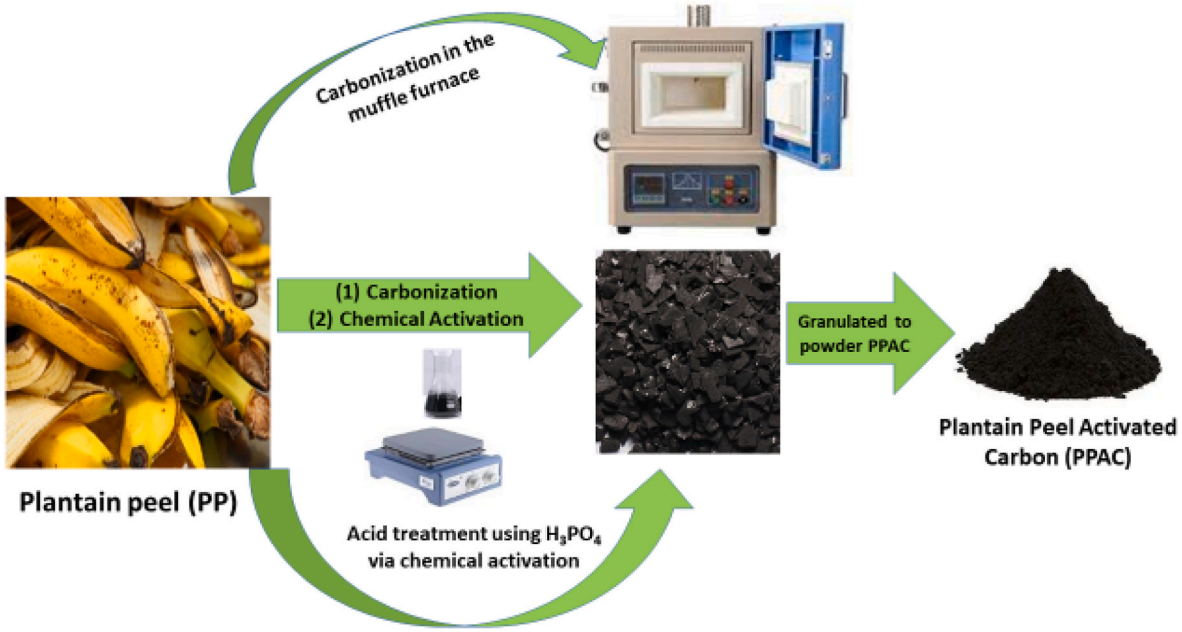

Scheme 1. Development of Plantain Peels Activated Carbon (PPAC).

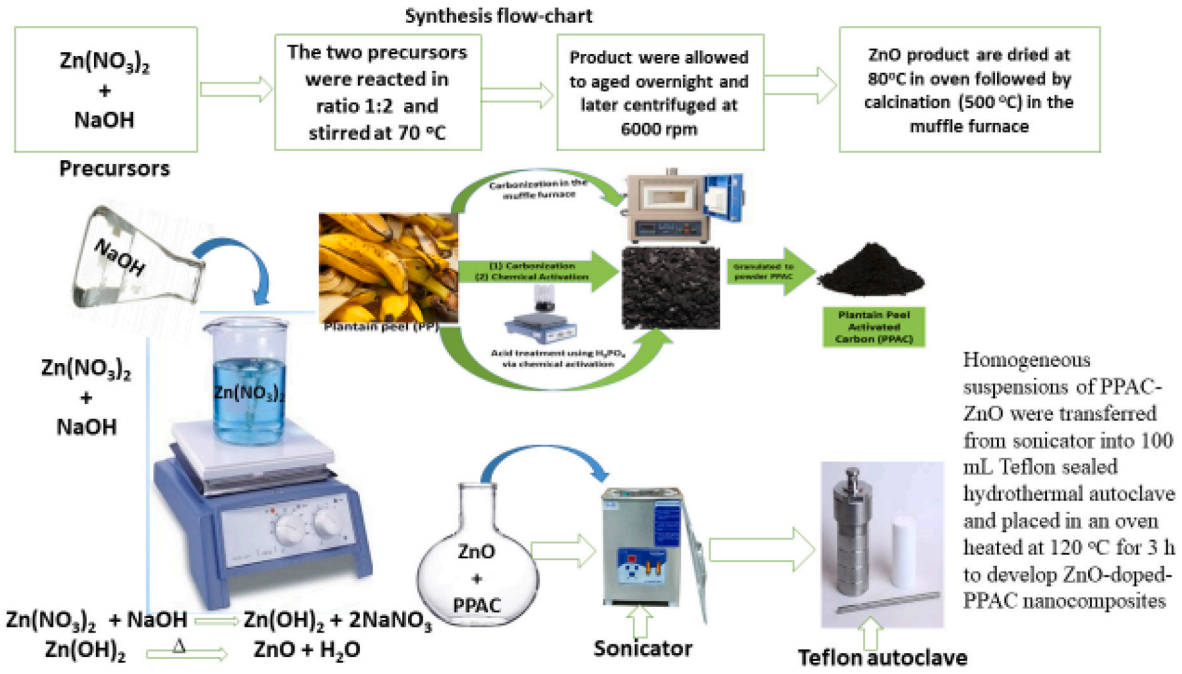

Scheme 2. flow chart scheme of synthesis of ZnO@PPAC doped. Contained in Section I of the electronic supplementary information (ESI) are the procedures for the determination of the porosity, surface area, and surface functionality by the Boehm method.

2020)(Zeng and Xue, 2019). The UV–Vis was utilized to check the MG dye residues in the adsorption system. Equation (1) was applied to determine the amount of adsorbed MG dye.

$$Qe = \frac{(C_o - C_e)\ V}{m} \quad (1)$$

Q_e denotes the sorption capacity (mg/g) of the adsorbent, C_e stands for MG's equilibrium concentration (mg/L), C_o represents the initial MG concentration (mg/L); V stands for the solutions volume (L); m represents the adsorbents mass (mg). The % removal efficiency of ZnO@PPAC was determined with equation (2).

$$Removal\ (\%) = \frac{C_o - C}{C_o} \text{ x } 100 \quad (2)$$

C_o represents the initial MG concentration while C stands for the final MG concentration (mg/L) after the sorption process.

Furthermore, various operational parameters were also monitored throughout the adsorption experiment. The influence of varying the initial pH on the adsorptive ability of the adsorbent was observed at pH values of 3, 5, 7, 9 and 11 (Inyinbor et al., 2016). These pH values were attuned by utilizing 0.1 M HCl and NaOH. The influence of time of contact between MG dye and ZnO@PPAC was varied and monitored at 10, 20, 30, 60, 90, 120 and 240 min. However, prior to equilibrium established, the change in residual adsorbate was monitored and documented using a UV–vis spectrophotometer (Sartape et al., 2017). A quicker pace at which MG dye molecules travel from the bulk and reach the inner and outer surface of ZnO@PPAC is shown by the shorter contact time required to attain equilibrium. It is thus a vital factor in the transfer course (Sudhakar and Soni, 2018).

The influence of various temperatures at 30, 40 and 50 °C on the sorption capacity of ZnO@PPAC was also observed. This adsorption characteristic is crucial since rising temperatures often lead to more adsorption sites and thinner boundary layers around adsorbents (Sartape et al., 2017).

The initial concentration is also a vital adsorption operational parameter as it offers the driving force (momentum) needed to surpass the adsorbate-adsorbent boundary resistance due to the mass transfer. The influence of varying the initial concentration (between 10 and 50 ppm) of MG dye on their adsorption by ZnO@PPAC was therefore monitored (Gündüz and Bayrak, 2017).

2.6. Adsorption Kinetics, isotherms, thermodynamics and statistical validity models

Models for isotherm studies describe the nature with which adsorbates and adsorbents relate throughout the adsorption experiment. In this research, the adsorption data were subjected to four isotherm models to ascertain which model best defines the uptake. The Dubinin-Radushkevich, Freundlich, Temkin and Langmuir isotherm models were used and presented in Table 1. Adsorption Kinetics data were also subjected to four mechanism and kinetic models. Described also in Table 1 are Intraparticle diffusion, Pseudo Second Order, Pseudo First Order and Elovich models (Bayode et al., 2020a), (Obayomi et al., 2023c).

Adsorption kinetic studies give important details on the adsorption reaction pathway and its mechanism. It describes that the adsorption rate is highly reliant on adsorbate concentration and studies the influence of the adsorption rate on the capacity of ZnO@PPAC.

The nature, feasibility, and spontaneity of the sorption process were studied via thermodynamics parameters. The monitored parameters in thermodynamic studies reveal the various energy changes that occurred in the course of the sorption experiment. In this research, three (3) thermodynamic parameters are assessed which are the Standard enthalpy change (ΔH^o), Standard free energy change (ΔG^o) and Standard entropy change (ΔS^o) as described in Table 1 (Dada et al., 2020a).

3. Results and discussion

3.1. ZnO@PPAC nanocomposites characterization

3.1.1. Physicochemical properties

ZnO@PPAC was discovered to have a pH value of 7.21, which is within the permitted range. According to reports, pH levels between 6 and 8 are suitable for wastewater decontamination purposes. The moisture, ash content and volatile matter contents of 7.54%, 12.18% and 31.48% were observed respectively for ZnO@PPAC. The low moisture content could be ascribed to the calcination step in the zinc

Table 1
Model equations of isotherms, kinetics and thermodynamics (Foo and Hameed, 2010; Dada et al., 2017a; Tokula et al., 2023b).

Models	Mathematical Expression	Plot axis	Slope	Intercept	Evaluated Parameters	Description
Isotherms models						
Langmuir	$\frac{Ce}{qe} = \frac{C_e}{Q_m} + \frac{1}{Q_m K_L}$ $R_L = \frac{1}{1 + K_L C_o}$	C_e/q_e *vs* C_e	$\frac{1}{Q_m}$	$\frac{1}{Q_m K_L}$	Q_m *and* K_L	q_e = amount of adsorbate adsorbed per unit mass of adsorbent(mg/g) C_e = equilibrium concentration of adsorbate (mg/L), C_0 = initial concentration of adsorbate (mg/L), K_L=Langmuir adsorption constant (L/mg), Q_m = monolayer sorption capacity of the adsorbent (mg/g)
Freundlich	$log\ Qe = log\ K_F + \frac{1}{n} log\ Ce$	log qe Vs log Ce	$\frac{1}{n}$	$log\ K_F$	$\frac{1}{n}$ *and* K_F	q_e = amount of adsorbate adsorbed per unit mass of adsorbent (mg/g) C_e = equilibrium concentration of the adsorbate (mg/L) K_f and n = Freundlich constant affiliated with the adsorption capacity and adsorption intensity respectively. $1/n$ = adsorption intensity 1/n = 0 is irreversible but 1/n > 1 is unfavorable 0 < 1/n < 1 favourable
Temkin	$Qe = BlnA_T + Bln\ Ce$	Qe Vs ln Ce	B	$BlnA_T$	A_T and B	A_T = equilibrium binding constant (L/mg) q_e = amount of adsorbate adsorbed at equilibrium (mg/g), $B = RT/b$ = Constant related to the heat capacity (L/mg) T = absolute temperature (K), R = Universal gas constant (8.314 J/mol/K), C_e = equilibrium concentration of adsorbate (mg/L)
D-R	$ln\ Qe = -\beta\varepsilon^2 + \ln Q_m$ $E = \frac{1}{\sqrt{2\beta}}$	ln q_e vs ε^2	$-\beta$	$\ln Q_m$	β *and* Q_m	B = Dubinin-Radushkevich constant, qe = amount of adsorbate adsorbed at equilibrium, T = absolute solution temperature R = universal gas constant, Qm = maximum adsorption capacity, Ce = adsorbate equilibrium concentration Physisorption if E is between 1 and 8 kJ/mol and chemisorption if E is between 9 and 16 kJ/mol.
Kinetics Models						
Pseudo first order	$\ln (q_e - q_t) = \ln q_e - k_1 t$	ln (q_e- q_t) Vs t	k_1	ln q_e	q_e and k_1	q_e and q_t are the quantities of adsorbed BPA at equilibrium and periods t, respectively. k1 denotes the pseudo-first-order rate constant.
Pseudo second order	$\frac{t}{q_t} = \frac{1}{h_2} + \frac{t}{q_e}$ t $h_2 = k_2 qe^2$	t/qe Vs t	$1/q_e$	$1/h$	q_e, k_2, h_2	k_2: pseudo-second-order rate constant, h_2 = initial adsorption rate.
Elovich	$q_t = \frac{1}{\beta} lnt + \frac{1}{\beta} ln(\alpha\beta)$	q_t Vs ln t	1/β	$\frac{1}{\beta} ln(\alpha\beta)$	α, β	∝ = initial adsorption rate (mg/g-min); β = desorption constant (g/mg) during any one experiment
Intraparticle diffusion	$q_t = K_{IPD} t^{1/2} + C$	q_t VS $t^{1/2}$	K_{IPD}	C	K_{IPD}, C	k_{ipd} is the intraparticle diffusion rate constant (mg.g1min0.5), and C is the intercept indicating adsorbent thickness. The q_t parameter is the amount of solute adsorbed per unit weight of adsorbent per time (mg/g), and $t^{1/2}$ represents the half-adsorption time.
Thermodynamics						
Gibbs Free Energy	$\Delta G^\circ = -$ RTlnKd				ΔG°	ΔG° is for Gibbs free energy change; Kd stands for the equilibrium constant; R stands for gas constant, and T stands for temperature.
Van't Hoff Plot	$\ln K_C = \frac{\Delta S}{R} - \frac{\Delta H}{RT}$	ln K_C versus $1/T$	ΔH^o	ΔS^o	ΔH^o, ΔS^o	ΔS^o = change in standard entropy (kJ/mol K), K_L=Langmuir adsorption constant (L/mg) R=Universal gas constant (8.314 J/mol K), T = absolute solution temperature (K), ΔH^o = change in standard enthalpy (kJ/mol K).
Arrhenius Equation	$\ln k_2 = \ln A - \frac{Ea}{RT}$	ln K_2 versus 1/ T,	E_a	A	A, E_a,	T = absolute temperature E_a = Arrhenius energy activation for adsorption (kJ/mol), K_2=PSO kinetic model rate constant (g/mg min). A = Arrhenius factor R = universal gas constant
Statistical Validity Model						
Sum of Square Error (SSE)	$SSE = \sum_{i=1}^{n} (q_{e,cal} - q_{e,\exp})^2$					q_e, exp is the experimental quantity adsorbed at equilibrium and q_e,cal is the quantity adsorbed calculated from the model equation.
Chi-square test χ^2	$\chi^2 = \sum_{i=1}^{n} \frac{(q_{e,\exp} - q_{e,cal})^2}{q_{e,cal}}$					

oxide nanocomposite synthesis. The produced activated carbon and its nanoparticles are suitable materials for use as adsorbents because they have a low volatile matter concentration which implies that they possess a low particle density (Ekpete et al., 2017). In adsorption experiments, the surface area is a crucial variable. It is expected that adsorbents with higher surface area would have better sorption capacity. As shown in Table 2, a specific surface area of 205.2 m^2/g was observed which shows that incorporating nanoparticles into the activated carbon had increased the surface area. This observed trend is reinforced by the findings of (Shayesteh et al., 2016; Xu et al., 2023) (see Table 3).

3.1.2. Surface porosity

The estimation of the surface porosity of ZnO@PPAC in the determination of its suitability for the uptake of large molecules was determined by iodine adsorption. The surface porosity of ZnO@PPAC nanocomposite is depicted in Fig. 1. The iodine number obtained for ZnO@PPAC gives the extent of its adsorptive capacity and porosity as well as an estimated surface area. The iodine number was determined to be 614.68, The high iodine number of 614.68 obtained suggests the existence of a large surface area and pores on the ZnO@PPAC surface (Atunwa et al., 2022) (Abdullah et al., 2018).

Table 2
Physicochemical characterization of ZnO@PPAC

Property	Value
pH	7.21
% Moisture	7.54
% Ash	12.18
% Volatile matter	31.48
Bulk density	0.65
pH_{pzc}	4.99
Surface area (Sears method)	205.2

Table 3
Oxygen Containing Functional groups.

Groups	ZnO@PPAC
Carboxylic (meq/g)	0.5
Phenols (meq/g)	0.4
Lactones (meq/g)	0.3
Total Acidic sites	1.2
Total Basic sites (meq/g)	0.9

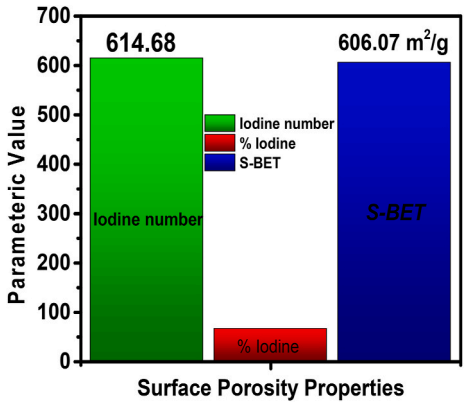

Fig. 1. Surface porosity of ZnO@PPAC nanocomposites.

3.1.3. Boehm technique for oxygen-containing functional group determination

The oxygen-containing functional groups on ZnO@PPAC were investigated via the Boehm titration method. The results displayed in Table 3 reveal that the ZnO@PPAC surface was predominantly acidic. The value obtained agrees with the pH Pzc value which was geared towards the acidic region. Due to this, the adsorption of cationic pollutants will be enhanced (Gündüz and Bayrak, 2017). Similar conclusions were drawn by Mudyawabikwa et al. (2017) who modified tobacco stems to activated carbon.

3.1.4. X-ray diffraction (XRD) analysis

The plot in Fig. 2 shows the lattice spherical distinguishing morphology of the pure ZnO pristine, and this is supported by the XRD pattern and FTIR surface chemistry analyses. This nanocomposite analysis was carried out to examine the crystalline nature of ZnO, PPAC, and ZnO@PPAC. The plantain peel is amorphous and not crystalline being an activated carbon precursor. Both ZnO and ZnO@PPAC showed prominent similar peaks at 32.15°, 34.76°, 36.71°, 47.90°, 56.88°, and 63.29° which indicates the formation of the zincite and wurtzite phase of ZnO (Dada et al., 2020b). The existence of additional peaks at 47.90°, 56.88°, and 63.29° despite the support of PPAC reveals a non-disruption of the phases of zinc oxide.

3.1.5. Fourier transform infrared analysis (FTIR)

FTIR analysis was performed to ascertain the already existing functional groups on the surface of Plantain Peels Unmodified (PPU), PPAC, ZnO and ZnO@PPAC as revealed in Fig. 3. The functional groups have been assigned as depicted in Fig. 3. The functional groups ascribed to PPU as found in 3393 cm^{-1}. 2914 cm^{-1}, 1645 cm^{-1}, 1370 cm^{-1}, 1033 cm^{-1} and 634 cm^{-1} are prominent hydroxyl group (OH), C–H, –C═O, -C-O, -C-O-H, -C-X respectively. The observed peaks at 3400 cm^{-1} suggest OH stretch which is because of polymeric compounds such as pectin or lignin-containing functionalities (alcohols, phenols, and carboxylic acid) (Ding et al., 2015; Deb et al., 2019). The developed plantain peel activated carbon (PPAC) has vibration bands with functional groups at 3383 cm^{-1} (reduced –OH), 2886 cm^{-1} (-C-C- str of alkane), 1592 cm^{-1} (-C═O-) carbonyl, 1220 cm^{-1} (-C-O-) stretching and –C-X bending. The disappearance of some functional groups in PPAC was a result of volatile organic matters that escaped during carbonization and the introduction of bonds during chemical activation. PPAC served as one of the precursors of ZnO@PPAC. From ZnO, the following peaks were observed: 3449 cm^{-1} (-OH), 2931 cm^{-1} (-C-H stretching), 2416 cm^{-1} (-C═C-) stretching, 1609 cm^{-1} (C═O-), 1361 (-N-H-), 856 cm^{-1} (-C-O-H) and ZnO nanoparticles was observed at 572 cm^{-1} (Obayomi et al., 2023a; Choudhary et al., 2020). Both PPAC and ZnO were incorporated in the hydrothermal technique to develop ZnO decorated PPAC forming ZnO@PPAC. The appearance and disappearance of functional groups

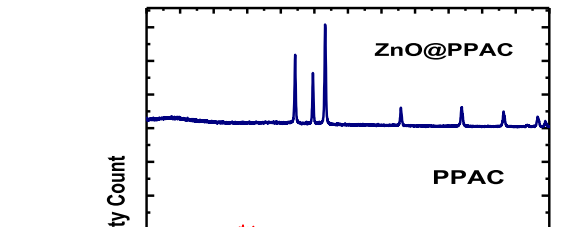

Fig. 2. XRD pattern of ZnO, PPAC and ZnO @PPAC.

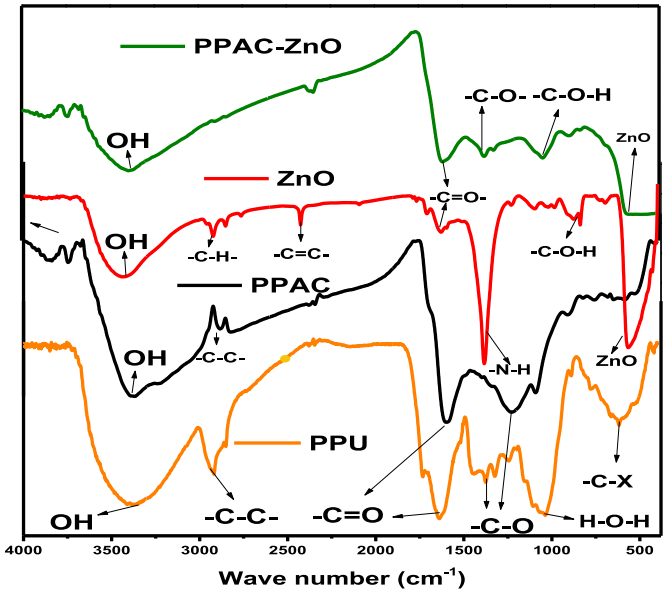

Fig. 3. FTIR spectra of Plantain peels unmodified (PPU), PPAC, ZnO and ZnO@PPAC

further supported the excellent development of ZnO@PPAC nanocomposites. The existing functional groups on ZnO@PPAC were identified by peaks around 3395 cm^{-1} matching the O–H stretch of alcohol. The C═C stretch at 2359 cm^{-1} was also observed. Peaks at 1616 cm^{-1} indicate the presence of –C═O of the lignin aromatic group, 1386 cm^{-1} allocated to C–O, 1030 cm^{-1} assigned to C–O–H (Bayode et al., 2020a; Zheng et al., 2020). The ZnO peak was also detected at 552 cm^{-1}. Similar peaks and trends were noted by Cruz et al. (2020) after loading ZnO onto the activated carbon.

3.1.6. SEM morphological studies

Scanning Electron Microscopy (SEM) was applied to ascertain the surface morphological variations in both the precursors and the nanocomposite. The plots in Fig. 4(a–f) are the SEM images with noticeable changes. Fig. 4(a) shows the morphology of the carbonized plantain peel revealing a shred, shrink and uncoordinated surface without evidence of pores arising from the heat application and evaporation of volatile organic matter. The obtained results were comparable to the reports of Dada et al. (2021) who investigated chloroquine adsorption using H_3PO_4 treated plantain activated carbon loaded zinc oxide nanocomposites. SEM image of the main precursor (PPAC) in Fig. 4(b) revealed various pores of different shapes and sizes with fine surface textures. These pores could be due to the chemical modification of the plantain peel. Fig. 4(c) shows a lattice spherical characteristic morphology of the pure ZnO pristine, and this is supported by the XRD pattern and FTIR surface chemistry analyses. Fig. 4(d and e) shows the morphology of the well-developed ZnO@PPAC nanocomposites. A great mesoporous morphological change was noticed as revealed in the successful incorporation of the PPAC into the matrix of ZnO for the formation of ZnO@PPAC nanocomposites. The illustrated reddish lines show the appearance of the homogenous incorporation of PPAC on ZnO. Also, the morphology of ZnO@PPAC nanocomposite revealed that PPAC did not disrupt the spherical structure of ZnO as evidenced by the XRD pattern and FTIR analyses. This was supported by our previous report where rice husk-activated carbon was successfully loaded on ZnO (Dada et al., 2022). Fig. 4(f) shows the SEM image of ZnO@PPAC loaded with malachite green dyes. The rupture of the spherical morphology and drastic change in the shape of ZnO@PPAC revealed that the MG dye molecule (endocrine disruptive dye) was trapped and swallowed in the porous pores as well as the trapping of the MG dye molecule (endocrine disruptive dye) participation of the pores in the adsorption process. This further supported that the pores also served as sites of adsorption for the uptake of MG pollutants as buttressed by other reported research (Sartape et al., 2017; Sudhakar and Soni, 2018).

3.1.7. TEM, HR-TEM, SAED, electromapping and EDX analysis

Transmission Electron Microscopy (TEM) is a strong, invaluable analytical tool for nanoparticle characterization. Fig. 5(a–f) and Fig. 6 (a–f) display the representative TEM and HR-TEM images of ZnO@PPAC nanocomposites. The morphology of ZnO which appears spherical is shown in Fig. 5(a) and 6(a). Similarly, the structure of ZnO@PPAC which is rod-like affirms its nano-rod-like structure. Furthermore, Fig. 5 (e and f) reveals the mesoporous nature of the heterostructure of ZnO@PPAC. The nanoparticle size was determined as 40–50 nm and 80–90 nm for pure pristine ZnO and ZnO@PPAC respectively using Image J software. Fig. 5(e and f) further affirms the interspatial lattice spacing of the ZnO@PPAC heterostructure. This corresponds to findings by (Gündüz and Bayrak, 2017; Lari et al., 2020; Obayomi et al., 2023c). Moreso, in order to confirm the elemental composition of ZnO@PPAC, elemental mapping via High Angular Dark Field Image (HAAF) was carried out. As shown in Fig. 6(b–e), the carbon is depicted in a yellow colour and is evenly distributed across the ZnO@PPAC. Similarly, Zinc is depicted by a red colour while oxygen is depicted by a green colour.

Furthermore, the Selected Area Electron Diffraction (SAED) pattern of ZnO@PPAC is displayed in Fig. 5(c and d) Images show the crystallinity of the heterostructured nanomaterial. Fig. 6(f) represents the EDX image showing elemental distribution at different peaks revealing the presence of carbon (C), zinc (Zn) and oxygen (O) and the intense peak of

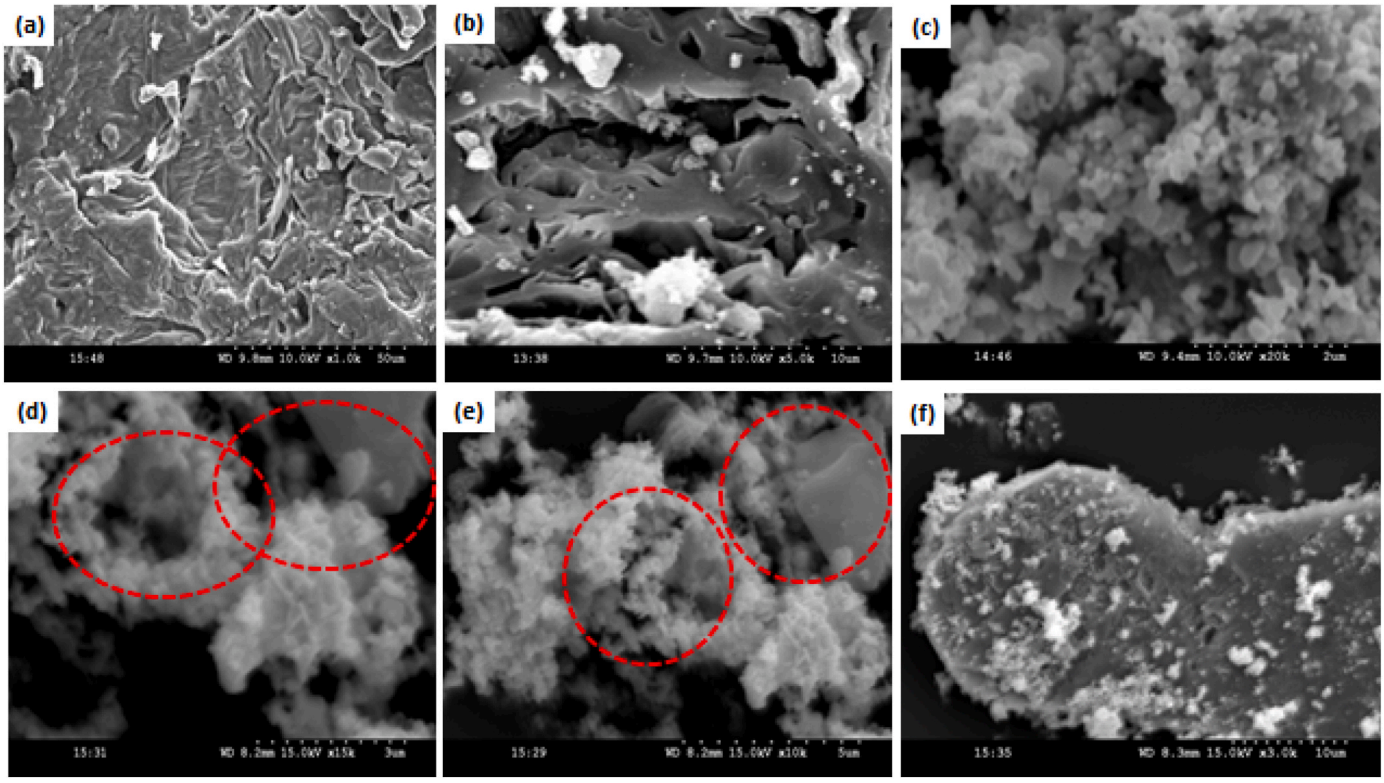

Fig. 4. (a–f): SEM morphology of (a) carbonized plantain peels (CPP) (b) Plantain peels activated carbon (PPAC) (c) Pure Pristine Zinc oxide (ZnO) (d) & (e) PPAC-ZnO before adsorption at different magnifications (f) ZnO@PPAC-MG system after adsorption.

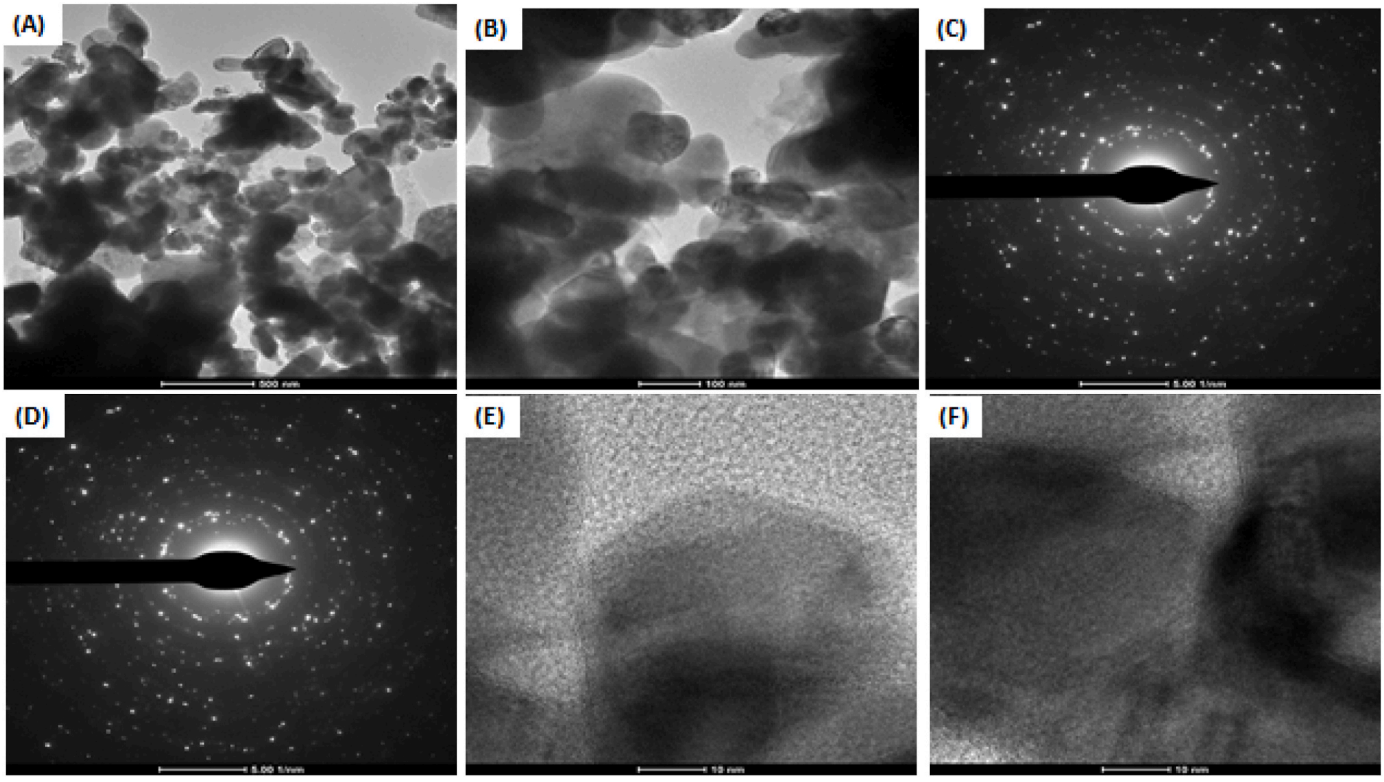

Fig. 5. (a–b) Typical TEM (c–d) SEAD pattern (e–f) H–R TEM of ZnO@PPAC

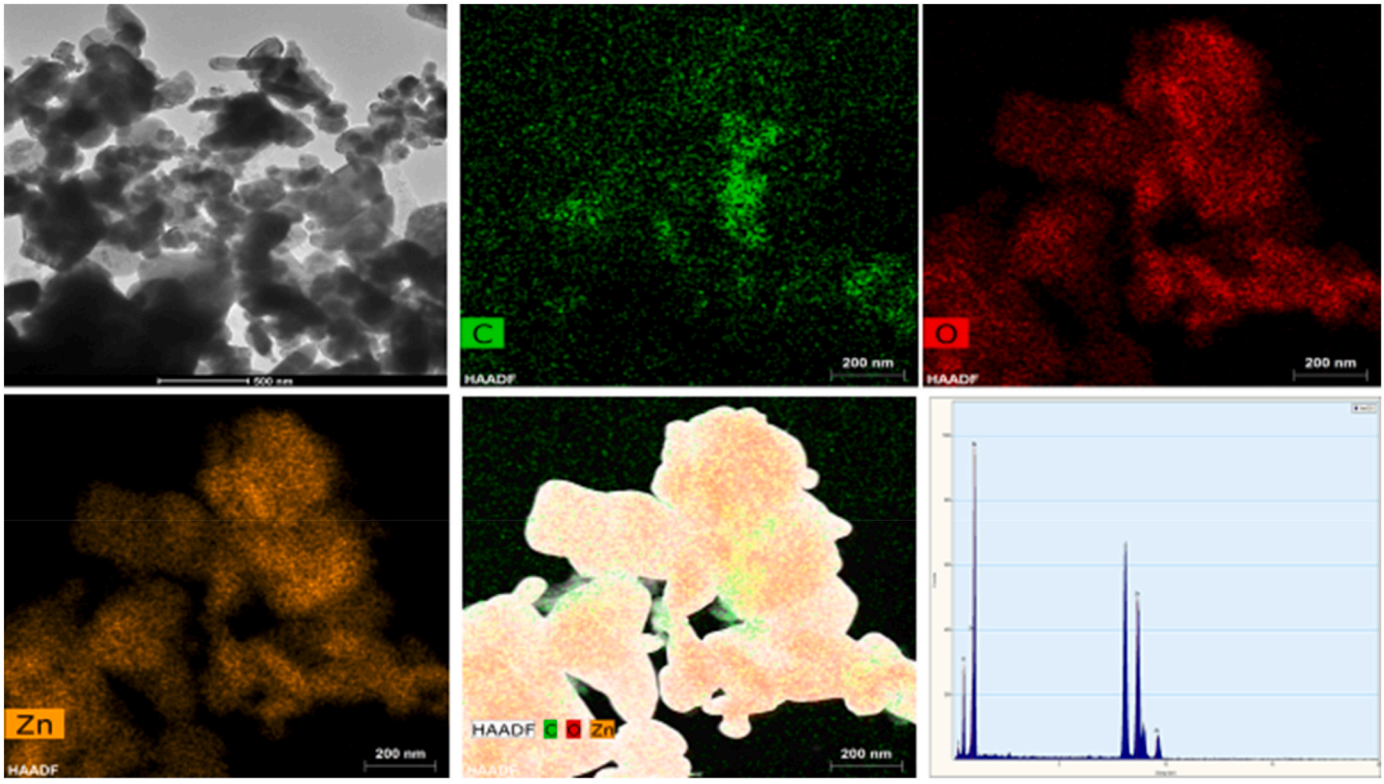

Fig. 6. (a) shows a typical TEM (b–e) High Angular Dark Field Image (HAAF) (f) EDX image showing elemental distribution at different peaks. of ZnO@PPAC

zinc and oxygen supporting the formation of ZnO.

3.1.8. TGA, DTG & DSC

To investigate the thermal stability of ZnO@PPAC, differential scanning calorimetry (DSC), thermal gravimetric analysis (TGA)

analyses and derivative thermogravimetry (DTG) were carried out as depicted in Fig. 7(a). There are three stages of phase changes and weight loss observed from the TGA plot. At the initial level, a weight loss of 8.54% was observed from 16 to 102 °C due to moisture evaporation. A decrease was however recorded between 102 and 500 °C and this resulted in a weight loss of 5.07 %. This loss is due to the hemicellulose material degradation, including volatile matter and cellulose (Kumar et al., 2020). The last stage of decrease was observed from 500 °C to 800 °C resulting in weight loss of 9.0% which could be accredited to lignin breakdown(Conde-rivera et al., 2021).

From the DTG curve, the highest peak loss was observed between 74 °C and thereafter, there was no significant change except the slight change observed between 600 and 779 °C. After this change, there was thermal stability in ZnO@PPAC. A comparable observation was made by Workie et al. (2019). DSC curve analysis depicts the heat flow as well as the thermal phase transition showing typically an exothermic transition of ZnO@PPAC at different crystallization peaks of 33 °C (−3.84 mW/°C), 77.8 °C (−8.84 mW/°C) and 191 °C (9.45 mW/°C). At elevated temperatures, the crystallinity of the ZnO@PPAC nanocomposite increases as confirmed by the XRD study before adsorption. This finding corresponds to the reports of (El-Naggar et al., 2020) where three transition peaks were observed on Chlorella Vulgaris polysaccharides and the study of (Saleh et al., 2017).

3.2. Adsorption studies

3.2.1. Synergistic influence of initial concentration and contact time

Malachite green (MG) dye uptake was systematically done and the synergistic studies of the influence of various operational parameters were examined. The influence of initial concentration in synergy with contact time for the sorption of MG was observed and represented in Fig. 8(a). A plot of quantity adsorbed (q_t) versus time (t) revealed the synergistic influence of initial concentration (10–50 mg/L) and contact time (5–240 min) on the sorption system. The adsorption process was rapid for the first 15 min. This could be attributed to the existence of additional active adsorption sites at the initial stages, the uptake then gradually became slower until equilibrium was attained between 180 and 240 min. This decline could be a result loading up of MG into the pores of ZnO@PPAC thereby making ZnO@PPAC sites unavailable for adsorption after the site saturation (Bayode et al., 2020a). This was confirmed by the spectroscopic analyses from SEM, XRD and FTIR.

3.2.2. Synergistic influence of temperature and initial concentration

As observed in Fig. 8(b)–a synergistic determination of the influence of temperature alongside the influence of initial MG dye concentration was explored. It was noted that a rise in the initial MG dye concentration led to a rise in the amount of MG dye adsorbed at a specific time (q_t). This could be attributed to the typical nature of an endothermic system. More so, this could also be due to the resultant rise in initial concentration gradient at more initial MG concentration leading to a rise in the driving force which helped to override the resistance due to mass transfer resulting in the rapid uptake of malachite green molecules. At the equilibrium point, the quantity of MG dye adsorbed onto ZnO@P-PAC at a 10 mg/L initial concentration was 6.4 mg/L, while at a 50 mg/L initial concentration, the quantity of adsorbed MG was 32.1 mg/L. A comparable trend was reported by Ojediran et al. (2020) who reported on the uptake of MG dye onto functionalized maize cob. The rise in temperature of the adsorption system led to a rise in the uptake of MG dye as shown in Fig. 8(b). This observed trend could be because of the obtainability of more adsorption sites at greater temperatures (Feng et al., 2024). Guechi & Hamdaoui (Guechi and Hamdaoui, 2016) reported a similar trend of results in the uptake of MG dye onto potato peel.

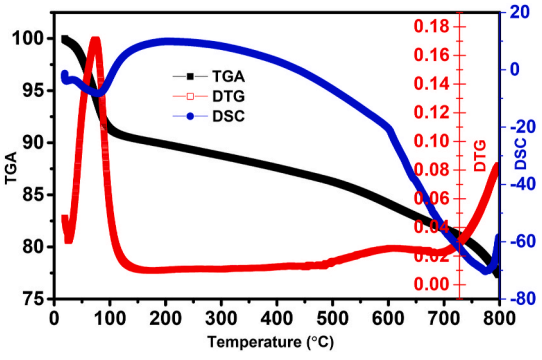

Fig. 7. TGA, DTG and DSC analysis of ZnO@PPAC

3.2.3. Influence of pH and $pH_{(PZC)}$

The Point of zero charge plot is depicted in Fig. 8(c). The $pH_{(PZC)}$ indicates the pH value at which the ZnO@PPAC surface has an overall neutral charge. This was carried out via the salt addition approach. The pH_{pzc} for ZnO@PPAC was 4.99 as depicted in Fig. 8(c). This implies that at pH values higher than 4.99, ZnO@PPAC has a negative charge and will be efficient in adsorbing cationic pollutants. Similarly, at pH values lower than 4.99, ZnO@PPAC has a positive charge and will be efficient to adsorb anionic pollutants (Masoudian et al., 2019; Abdullah et al., 2018). This is imperative in studying the pH influence on the MG adsorption onto ZnO@PPAC-Nanocomposite. Fig. 8(d) depicts the influence of solution pH on the uptake of MG onto ZnO@PPAC which was done at pH values ranging from pH 3–11. As a basic dye, MG forms cations in solution (Choudhary et al., 2020). ZnO@PPAC had the highest percentage removal of 87.9 % at pH 7. The high percentage removal could be a result of the negative charges existing on the ZnO@PPAC surface at pH values greater than pH_{pzc} which results in the attraction between ZnO@PPAC-NC's surface (He et al., 2024) and MG molecules resulting in an increase in uptake at this region (Mudyawabikwa et al., 2017). However, at pH values less than the pH point of zero charge, the ZnO@PPAC surface becomes positively charged which causes a repulsion between MG molecules and the surface of ZnO@PPAC, thereby reducing the MG uptake in this region as can be observed in Fig. 8(c). Wang et al. (2019) observed and reported comparable results on MG dye decontamination using natural zeolite.

3.3. Isotherm studies

Isotherm studies were employed to further comprehend the nature of the interactions between the adsorbent-adsorbate interface and all adsorption systems. The equilibrium study was investigated at three different temperatures unlike the common convectional where the interaction is carried out at only one temperature. This research reports that sufficient equilibrium data obtained were fitted to Dubinin-Raduskevich. Langmuir, Temkin and Freundlich isotherm models.

The Langmuir isotherm adopts that as distance increases, a swift reduction of intermolecular forces occurs. Langmuir also envisages that the coverage nature of the adsorbate (MG dye) on the surface of ZnO@PPAC is a monolayer. Freundlich isotherm model assumes a heterogeneous and multilayer adsorption due to differences in sorption sites (Agboola and Bello, 2020; Sridhar et al., 2018). The Temkin model explicitly considers MG dye- ZnO@PPAC interactions and does not consider the exceptionally small and extremely large values for concentration (Dada et al., 2023). It assumes that the heat of adsorption (function of temperature) of all molecules of MG dye, instead of decreasing logarithmic, will decrease linearly with coverage (Foo and Hameed, 2010). The D–R isotherm is used to describe the mechanism of sorption onto a heterogeneous surface with a Gaussian energy distribution (Lazim et al., 2021; Ali et al., 2018; Dada et al., 2017b. It is used to differentiate the physisorption and chemisorption for the removal of a molecule of MG dye from its position in the adsorption space to an infinite point (Foo and Hameed, 2010). The equilibrium data were

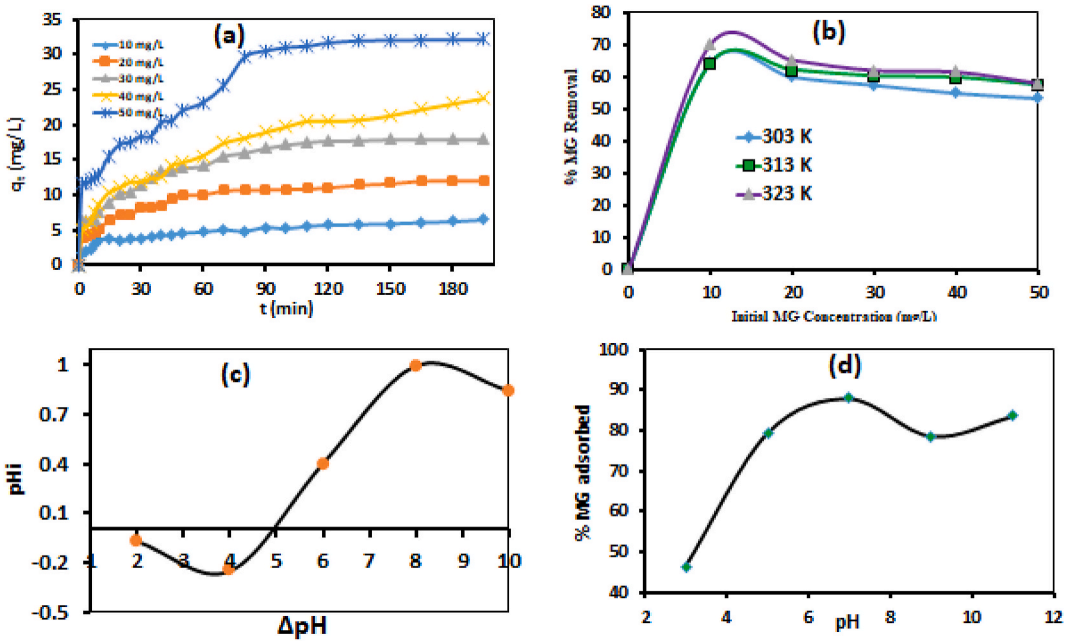

Fig. 8. Effect of (a) contact time at various concentrations (b) initial concentration at various temperatures (c) Point of Zero charges and (d) pH for the uptake of MG onto ZnO@PPAC

obtained from the plots of several adsorption isotherm models (Dubunin-Radushkelvich, Freundlich, Temkin, and Langmuir) at three (3) temperatures (303 K, 323 K and 313 K). The plot of the best-fitted data considered in this study is shown in Fig. 9. Outlined in Table 4 are the various appraised parameters at 303 K–323 K. For the ZnO@PPAC -MG system, the R_L value was found to be 0.25 (less than 1) this implies that the uptake of MG onto ZnO@PPAC is favourable. The highest monolayer capacity of adsorption (q_{max}) was obtained as 77.51 mg/g. The Freundlich isotherm best fitted the adsorption data with 0.99 as a high R^2 value, therefore implying that heterogeneous adsorption took place. The physical nature and favourability of the adsorption were expressed by the n values (greater than 1). The Temkin Isotherm plot obtained an R^2 value of 0.95 suggesting the presence of adsorbate-adsorbent interaction in the sorption process. The D-R plot gave a low R^2 value (0.86). However, the adsorption Energy of 0.71 kJ/mol (less than 8 kJ/mol) shows that the sorption of MG onto ZnO@PPAC was physio-sorption. Table 5 further outlines a vivid comparison among the highest monolayer capacity of adsorption of adsorbents in this study to several reported agro wastes and nanocomposites for MG Dye uptake. Obviously, the high Qmax of ZnO@PPAC compared to other previously reported adsorbents showed its efficiency, efficacy and superiority of other adsorbents reportedly used for MG adsorption.

3.4. Kinetic studies and statistical validity studies

Kinetic studies were performed to study the adsorption rate as well as

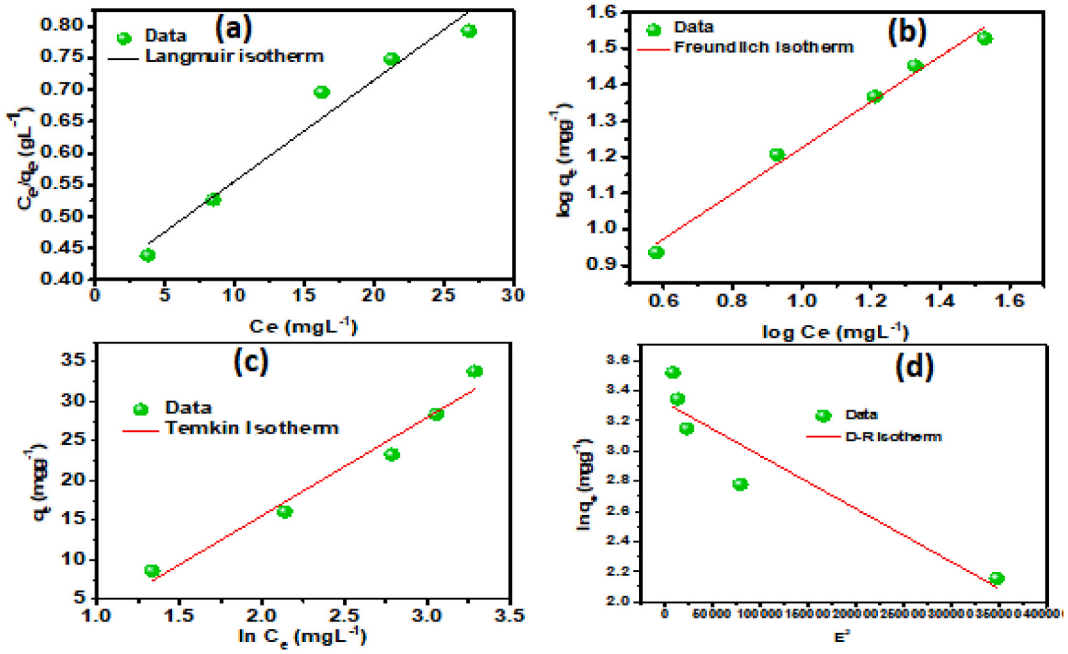

Fig. 9. (A)Langmuir (B) Freundlich (C)Temkin and (D) D-R linear Isotherm plots for MG-ZnO@PPAC.

Table 4
Adsorption isotherm parameters for uptake of MG using PPAC-ZnO-NC at different temperatures.

Isotherm	Parameters	303 K	313 K	323K
Langmuir	q_m (mg/g)	57.803	62.893	77.519
	K_L (L/mg)	0.0530	0.0400	0.0570
	R_L	0.272	0.332	0.257
	R^2	0.986	0.965	0.958
Freundlich	K_f (mg/g(L/mg))1/n	3.961	3.550	4.994
	N	1.456	1.462	1.339
	R^2	0.999	0.996	0.998
Temkin	B_T	228.110	217.284	193.333
	K_T	1.597	2.0880	1.128
	R^2	0.975	0.968	0.951
D-R	E_a (kJ/mol)	500.000	353.553	707.106
	q_m (mg/g)	24.818	27.699	27.560
	R^2	0.865	0.881	0.859
	$\beta \times 10^{-6}$ (mol^2kJ^{-2})	2.000	4.000	1.000

Table 5
Comparison of the Qmax (monolayer capacity) of ZnO@PPAC with other adsorbents for MG Dye removal.

S/N	Adsorbent	Qmax (mg/g)	Reference
1	Polylactide/Spent Brewery Grains Films	1.46	Chanzu et al. (2012)
2	Tamarind fruit shell	1.95	Saha et al. (2010a)
3	Coir Pith Activated Carbon (CPAC)	4.4	Arumugam et al. (2019)
4	PAC/Chitosan/SDC	4.8	Arumugam et al. (2019)
5	Chitosan ionic liquid beads	8.07	Naseeruteen et al. (2018)
6	Chitosan Zinc oxide composite	11	Muinde et al. (2020)
7	NaOH-modified rice husk	15.5	Chowdhury et al. (2011)
8	Fe_2O_3 by ODH	15.72	Dehbi et al. (2020)
9	Fe_2O_3 by PEG	16	Dehbi et al. (2020)
10	*Aegle marmelos* shell (AMS)	18.86	Selvasembian and Balasubramanian (2018)
11	Carbon prepared from Borassus bark	20.7	Arivoli et al. (2009)
12	*Annona squmosa* seed-activated carbon	25.9	Santhi et al. (2011)
13	Hen feather	26.1	Mittal (2006)
14	Leaves of Solanum tuberosum	33.3	Gupta et al. (2016)
15	Corn Cob (unfunctionalized)	35.34	Gan et al. (2017)
16	Wood Apple Shell	34.56	Sartape et al. (2017)
17	Pomegranate peel	31.5	Gündüz and Bayrak (2017)
18	Potato Peel	32.39	Guechi and Hamdaoui (2016)
19	Native shells of *Peltophorum pterocarpum*	40	Rangabhashiyam and Balasubramanian (2018)
20	Cellulose	40.9	Yildirim and Acay (2020)
21	*Musa* sp. Peel (MSP)	47.61	Selvasembian and Balasubramanian (2018)
22	Carica Papaya Wood	52.63	Rangabhashiyam et al. (2018)
23	Degreased coffee beans	55.3	Baek et al. (2010)
24	Mushroom	61.73	Yildirim and Acay (2020)
25	NaOH-activated shells of *Peltophorum pterocarpum*	62.5	Rangabhashiyam and Balasubramanian (2018)
26	SSB/Fe–Cu	63.5	Blanco-Flores et al. (2020)
27	Maize cob	64.51	Ojediran et al. (2021)
28	Functionalized Zea Mays Cob	64.52	Ojediran et al. (2020)
29	**ZnO@PPAC**	**77.51**	**This study**

the ZnO@PPAC–MG-adsorbate interactions. To prove the kinetics model's authenticity, the Sum of Square Error (SSE) and the Chi-square (χ^2) validity models were utilized. The validity of kinetic models is important as the regression coefficient (R^2) may not be a good judge of which model will most accurately describe the rate-determining step and mechanism (Thi et al., 2023; Dada et al., 2023). Plots of the pseudo-second-order (PSO), Elovich and pseudo-first-order (PFO) were made as depicted in Fig. 10(a–c). Table 6 outlines the determined kinetic model parameters. The R^2 values, the sum of square error (SSE) and chi-square (χ^2) and values were utilized to ascertain which of the Kinetic models best fit the sorption system. For the pseudo-first-order, low SSE values, lower χ^2 values and the negligible difference between the q_e calculated and q_e experimented value was observed for the removal of MG. However, the R^2 values for the PSO kinetic model across all concentrations were nearer to 1 than all other kinetic models. R^2 values ranged from 0.97 to 0.99 across all concentrations for all adsorption systems. The values of β decrease as concentration increases and the values of α which relate to the chemisorption rate are noticed to increase as concentration increases. This indicates that more than one mechanism may govern the uptake. The lower R^2 values obtained for Elovich and PFO kinetic models along with the higher SSE values and higher χ^2 values along with the larger difference between the experimental q_e values and the calculated q_e values make the Elovich and PFO kinetics models not fit for explaining the adsorption data. Based on the nearness of the q_e experimental and the calculated q_e values. The PSO was the kinetic model of the finest fit for the adsorption experiment. The kinetic models of best fit, therefore, followed the order PSO > Elovich > PFO. A similar trend was reported by (Sartape et al., 2017) who sequestered MG using wood apple shells.

3.5. The intraparticle diffusion model (IPD) mechanism

The intraparticle diffusion model parameters and plots are shown in Fig. 10 (D). The data utilized were deduced from the line equation of the plot of q_t versus $t^{1/2}$. For all initial adsorbate concentrations, the IPD plots did not cut over the origin as can be seen from the non-zero intercept (C) values outlined in Table 5. The non-zero intercept obtained for nearly all adsorbent-adsorbate interactions proposes that the rate-limiting step is determined by the IPD but apparently may not be the only mechanistic explanation for the MG uptake (Foo and Hameed, 2010; Ekpete et al., 2017). The observed rise in values of C as concentration increases shows that there was a rise in the effect at the boundary layer as the initial concentration increases. The boundary layer diffusion is another likely mechanism for the diffusion of the pharmaceutical molecules into the adsorbent materials. The values obtained for boundary layer thickness (C) and K_{diff} were noticed to rise generally as initial MG dye concentration increased suggesting a consequent increase in the boundary layer effect. The capacity of adsorbent material to adsorb or retain MG in solution is greatly influenced by these parameters (Bello et al., 2019a).

3.6. Thermodynamic studies

Thermodynamic studies were determined to shed more light on the adsorption's nature, feasibility, and spontaneity. The parameters relevant to the adsorption thermodynamics were determined and evaluated using Eq. 12. Fig. 11 depicts Van't Hoff's linear plot of ln K against 1/T from where the enthalpy and entropy were respectively obtained from the intercept and slope of the linear plot. The Values of Gibb's free energy was obtained from appropriate fitting and substitution using Eq. 13. Based on Table 6, the thermodynamics parameters of the amount of MG removed by ZnO@PPAC-NC between temperatures 303 K–323K as obtained from the linear plot of ln KL versus the reciprocal of temperature T (K) depicts positive value of ΔH as +52.062 kJ/mol showcasing the endothermic and favourable adsorption nature. ΔS nature found as 250.741 J/mol)/K demonstrated better equilibration, interaction, and randomness of the adsorbate MG with ZnO@PPAC-NC. Another important thermodynamics parameter is Gibb's free energy change, ΔG. Based on Table 7, the value of ΔG showcased negative values of (−29.258 kJ/mol) – (−24.203 kJ/mol) across all experimental temperatures portraying the spontaneity and feasibility of the sorption processes. The observed rise in temperature implies that temperature rise has a significant impact on thermodynamics. The energy of activation Ea was evaluated using Arrhenius eq. 13 from the linear plot's slope. This gives an idea of the type of adsorption to be classified as

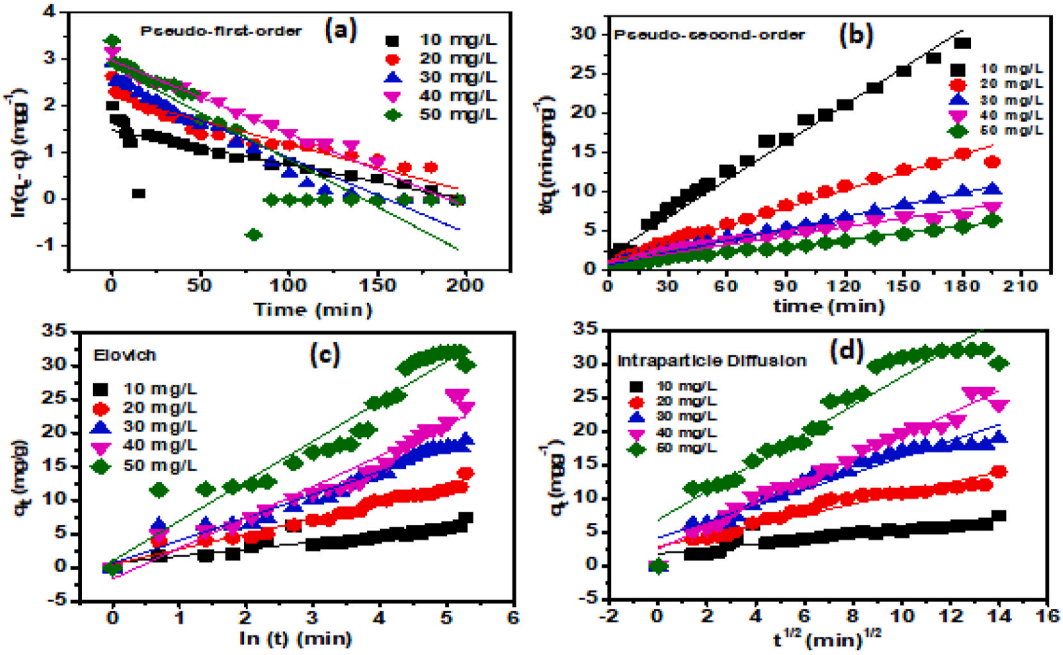

Fig. 10. Plot of (a) PFO (b) PSO (c) Elovich (d) IPD for ZnO@PPAC Nanocomposites system.

Table 6
Parameters of kinetic model for MG uptake using ZnO@PPAC

Model	Initial MG concentration (mg/L)				
	10	20	30	40	50
PFO					
$q_{e(exp)}$(mg/L)	7.459	14.042	18.943	23.894	30.113
$q_{e(cal)}$(mg/L)	4.419	9.026	12.121	19.601	17.312
k_1(min^{-1})	0.007	0.01	0.016	0.015	0.02
R^2	0.701	0.915	0.942	0.981	0.797
SSE (%)	9.238	25.156	46.552	18.426	163.867
χ^2	2.09	2.786	3.841	0.94	9.465
PSO					
$q_{e(exp)}$(mg/L)	7.459	14.0424	18.943	23.893	30.113
$q_{e(cal)}$(mg/L)	6.281	13.1926	19.685	26.455	34.482
k_2($gmg^{-1}min^{-1}$)	0.012	0.00479	0.0032	0.0013	0.0017
R^2	0.983	0.9833	0.991	0.956	0.981
SSE (%)	1.387	0.722	0.549	6.558	19.094
χ^2	0.221	0.0547	0.0279	0.247	0.553
Elovich					
B	0.955	0.441	0.292	0.218	0.168
A	2.063	2.866	4.148	6.514	7.08
R^2	0.817	0.966	0.966	0.934	0.925
Intraparticle-Diffusion					
C	1.816	2.885	4.165	2.547	6.885
k_{diff}	0.363	0.793	1.201	1.680	2.122
R^2	0.763	0.916	0.925	0.978	0.918

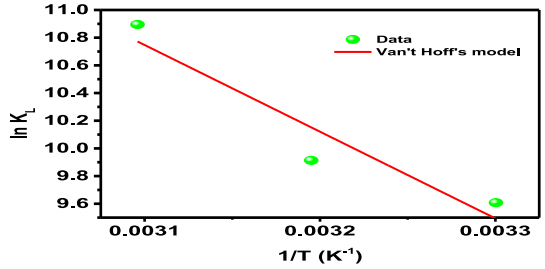

Fig. 11. Van't Hoff Plot for the adsorption of MG onto ZnO@PPAC

Table 7
Outlined thermodynamics data for the adsorption of MG onto ZnO@PPAC-NC

T (K)	ΔG^o (kJ mol^{-1})	ΔH^o (kJ mol^{-1})	ΔS^o (J mol^{-1} K^{-1})	E_a (kJ/mol)
303	−24.203			54.581
313	−25.798	52.062	250.741	54.664
323	−29.258			54.747

either chemisorption or physisorption based on the magnitude of the Ea. Physisorption adsorption is generally less than 40 $kJmol^{-1}$. The magnitude of the value of Ea being 54.747–54.581 kJ/mol across all temperatures demonstrated the adsorption process's mechanism to be chemisorption. This is an indication of a stronger force involved in the adsorption of the system (Saha et al., 2010b) A comparable trend in thermodynamic parameters was noted by Quesada et al. (2019) who examined the use of modified Moringa Olifera Seed Husk for adsorptive uptake of acetaminophen.

3.7. Adsorption mechanism of malachite green onto ZnO@PPAC

To further comprehend the adsorption mechanism of malachite green onto ZnO@PPAC some characterizations like FTIR, XRD and SEM of the pristine and spent adsorbents were carried out as presented in Fig. 12.

The extreme peak at 3400 cm^{-1} indicates the OH group reduced after MG dye adsorption has taken place suggesting the correlation between the OH group and MG dye molecules as seen in Fig. 12(a). The peak sandwiched between 3000 and 2500 cm^{-1} indicates that the C–H alkane stretching disappeared completely after MG dye adsorption. Interestingly, the development of a fresh peak at 2358 cm^{-1} was observed suggesting the existence of a C–O stretching band of amine, carboxylic acids and aromatic alcohols. The sharp peak at 1380 cm^{-1} indicated the OH bending reduced significantly after the adsorption while the peak at 706 cm^{-1} disappeared completely. All these changes confirmed that the OH group and C═O group contributed to the uptake of the MG dye (Wang et al., 2024b).

The SEM image of ZnO@PPAC loaded with malachite green dyes. The rupture of the spherical morphology and drastic change in the shape of ZnO@PPAC revealed that the MG dye molecules (endocrine

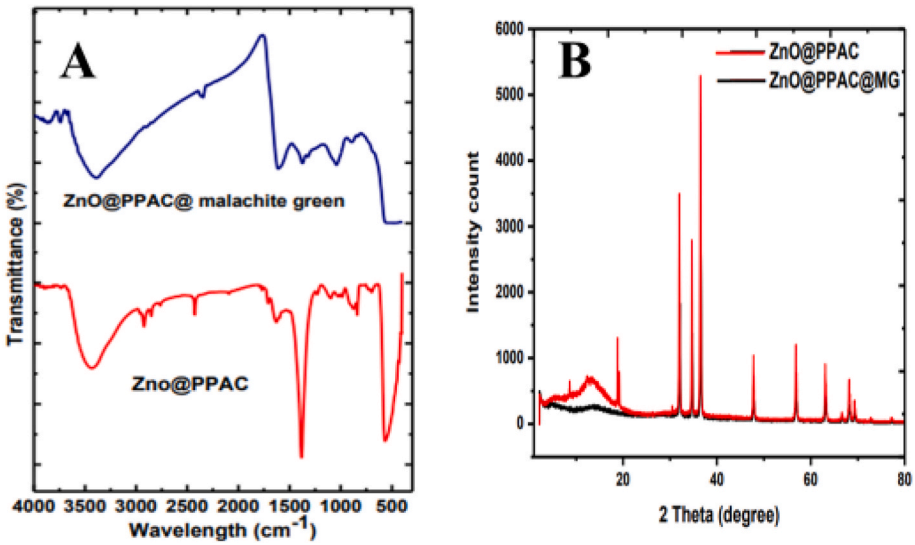

Fig. 12. A. FTIR, B. XRD of ZnO@PPAC before and after adsorption.

disruptive dye) were trapped and swallowed in the porous pores in the adsorption process. This further supported that the pores also served as sites of adsorption for the uptake of MG pollutants as supported by reports from the literature (Sartape et al., 2017; Dada et al., 2023).

The XRD of the pristine and spent adsorbent revealed that the intensity of the crystal phase of the zinc oxide reduced significantly confirming that it contributed greatly to the uptake of MG dye as seen in Fig. 12(b). Based on the analysis above, it could be established that the uptake of malachite green onto the adsorbent ZnO@PPAC, the shift and reduction in the peak intensity might be through various mechanisms such as interaction (electrostatic) between the MG dye molecule and the carboxylate ion on the ZnO@PPAC surface. Weak forces like the van Der Waals forces and hydrogen bonding between the MG dye on the ZnO@PPAC's surface and the nitrogen atom of the hydroxyl group.

Malachite green present in water interacts with functional groups such as hydroxyl (-OH), carboxyl (-COOH), and other polar groups on the surface of **ZnO@PPAC**. This provides active sites for interaction through various chemical interactions such as hydrogen bonding, electrostatic interactions, and van der Waals's forces. Electrostatic interaction happens when the adsorbent surface and adsorbate carry opposite charges (Xue et al., 2023). Cations are attracted to these sites if the surface has a negative charge. This results in cationic and anionic exchanges between the positively charged surface sites and negatively charged adsorbate. Cationic dyes will be adsorbed through cationic exchange when the surface is negatively charged. The SEM analysis confirmed the rupture of the spherical morphology and drastic change in the shape of **ZnO@PPAC**, which revealed that the MG dye molecule was trapped and swallowed in the porous pores. Additionally, the pores participated in the adsorption process and served as adsorption sites to uptake MG pollutants. This was confirmed by the effect of the pH experiment in section 3.2.3, as shown in Fig. 13 below.

3.8. Economic evaluation

One of the important parameters which could make adsorbent to be attracted industrialists is the issue of cost. This is seldom reported by the researcher as their focus is only on the performance of the adsorbent. The general production cost of adsorbent is principally based on the availability or the nature of the starting material (whether it be a waste or not). The popular commercial activated carbon costs a minimum of USD 259.5 as reported by Bello et al. (2019) (Bello et al., 2019b). Hence, this high cost limits its constant usage and availability. However, the cost of ZnO@PPAC is reduced due to the availability of the starting material at little or no cost. Table 8 shows a breakdown of the cost evaluation for the preparation of 1 g of ZnO@PPAC (2 USD) taking into consideration parameters like electricity, equipment, chemicals, etc.

Table 8
Cost evaluation of preparation of 1 g ZnO@PPAC

Materials/Chemicals/Equipment	Cost ($USD)
Plantain peel waste collection	–
Plantain peel waste pretreatment and activation	0.50
Electricity (Furnace, oven, centrifuge, sonicator, and hotplate	1.0
Reagent (H3PO4, zinc nitrate, and ethanol	0.50
Approximate total	2.0

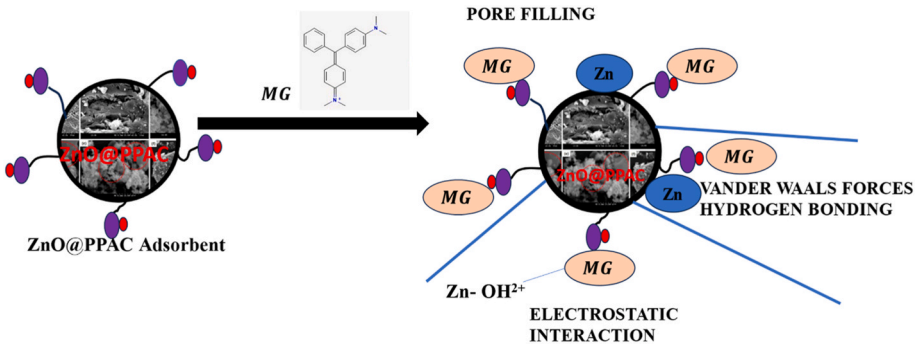

Fig. 13. A scheme showing the plausible mechanism of adsorption of malachite green dye onto ZnO@PPAC adsorbent.

In addition, the adsorption capacity of ZnO@PPAC was compared to previously reported adsorbents for MG dye decontamination as shown in Tables 4 and it proved to be very efficient as it has a good adsorption capacity of 77.51 mg/g. The adsorbents are economical because the parent material plantain peel is abundant in the environment as waste, it also serves as a means of waste conversion "waste to wealth".

4. Conclusion

In this study, ZnO@PPAC was successfully synthesized by hydrothermal technique. ZnO@PPAC was demonstrated to be an effective sorbent for MG dye decontamination from water with a maximum monolayer capacity of 77.517 mg/g. The various physicochemical and spectroscopic characterization processes enhanced the surface characteristics and pore structure thereby positioning ZnO@PPAC as an effective nanocomposite adsorbent. The SEM results revealed the existence of pores on the ZnO@PPAC surface, which proposes that sorption through the pores is one of the mechanisms for the uptake of MG dye in water. The FTIR, XRD and HR-TEM established the effective doping of the ZnO on PPAC. During the batch adsorption studies, fast and rapid adsorption happened around the first 40 min and progressively became slower until equilibrium was attained within 180–300 min. Synergistic operational parameters influenced the batch adsorption studies. The PSO Kinetics model was the best fit for the equilibrium data and the Langmuir isotherm model as observed from the similarity between experimental Q_e and calculated Q_e values, low SSE, and a high regression coefficient (R^2). Thermodynamics study showed that all sorption processes were spontaneous, favourable, and endothermic with a rise in randomness at the MG dye- ZnO@PPAC interface. The E values from the thermodynamics parameters and D-R plot also showed that physisorption was the dominant mode of adsorption. In conclusion, it can be inferred that ZnO@PPAC is effective for the uptake of MG dye. Based on the limitations of this research, we strongly recommend that the uptake of MG should be studied using real-life industrial effluent and desorption/reusability studies on these adsorbents should be carried out.

CRediT authorship contribution statement

Adewumi Oluwasogo Dada: Methodology, Conceptualization, Supervision, Validation, Writing – original draft, Writing – review & editing, Data curation, Formal analysis, Investigation, Project administration, Resources, Software. **Abosede Adejumoke Inyinbor:** Investigation, Writing – review & editing. **Blessing Enyojo Tokula:** Investigation, Methodology, Supervision, Writing – original draft. **Abiodun Ajibola Bayode:** Data curation, Investigation, Writing – review & editing. **Kehinde Shola Obayomi:** Writing – review & editing. **Christiana Oluwatoyin Ajanaku:** Writing – review & editing. **Folahan Amoo Adekola:** Writing – review & editing. **Kolawole Oluseyi Ajanaku:** Formal analysis, Writing – review & editing. **Ujjwal Pal:** Resources, Writing – review & editing.

Declaration of competing interest

The authors declare that they have no known competing financial interests or personal relationships that could have appeared to influence the work reported in this paper.

Data availability

Data will be made available on request.

Acknowledgements

This study was supported by the Postdoctoral Fellowship of The World Academic of Science with the Council of Scientific and Industrial Research (TWAS-CSIR) provided to Adewumi O. Dada, with code FR:3210316962. This provided the privilege to carry out some spectroscopic characterization. The enabling research environment provided by the Management of Landmark University is appreciated.

References

Abdullah, A.N., Abdullah, S.P., Amin, M.F.M., Zainol, A.N., 2018. Preparation and characterization of a new biocarbon material derived from Macaranga gigantea (giant ' Mahang ') leaf biomass as precursor. Mater. Today Proc. 5, 21888–21896. https://doi.org/10.1016/j.matpr.2018.07.047.

Abewaa, M., Mengistu, A., Takele, T., Fito, J., Nkambule, T., 2023. Adsorptive removal of malachite green dye from aqueous solution using Rumex abyssinicus derived activated carbon. Sci. Rep. 1–16. https://doi.org/10.1038/s41598-023-41957-x.

Adegoke, K.A., Bello, O.S., 2015. Dye sequestration using agricultural wastes as adsorbents. Water Resour. Ind. 12, 8–24. https://doi.org/10.1016/j.wri.2015.09.002.

Adekola, F.A., Ayodele, S.B., Inyinbor, A.A., 2019. Activated biochar prepared from plaintain peels: characterization and Rhodamine B adsorption data set. Chem. Data Collect. 19, 100170 https://doi.org/10.1016/j.cdc.2018.11.012.

Adeolu, A., Okareh, O., Dada, A., 2016. Adsorption of Chromium ion from industrial effluent using activated carbon derived from plantain (Musa paradisiaca) wastes. Am. J. Environ. Prot. 4, 7–20. https://doi.org/10.12691/env-4-1-2.

Agboola, O.S., Bello, O.S., 2020. Enhanced adsorption of ciprofloxacin from aqueous solutions using functionalized banana stalk. Biomass Convers. Biorefinery. https://doi.org/10.1007/s13399-020-01038-9.

Ahmed, M.B., Zhou, J.L., Ngo, H.H., Johir, A.H., Sornalingam, K., 2017. Sorptive removal of phenolic endocrine disruptors by functionalized biochar : competitive interaction mechanism , removal efficacy and application in wastewater. Chem. Eng. J. https://doi.org/10.1016/j.cej.2017.11.041.

Ali, I., Alharbi, O.M.L., Alothman, Z.A., Alwarthan, A., 2018. Facile and eco-friendly synthesis of functionalized iron nanoparticles for cyanazine removal in water. Colloids Surfaces B Biointerfaces 171, 606–613. https://doi.org/10.1016/j.colsurfb.2018.07.071.

Alipanahpour Dil, E., Ghaedi, M., Asfaram, A., Mehrabi, F., 2019. Fardin Sadeghfar, Efficient adsorption of Azure B onto CNTs/Zn:ZnO@Ni2P-NCs from aqueous solution in the presence of ultrasound wave based on multivariate optimization. J. Ind. Eng. Chem. 74, 55–62. https://doi.org/10.1016/j.jiec.2018.12.050.

Anna, T., Jens, K., Olov, E., Thomas, A., Schroder, E., 2018. Removal of phenol and chlorine from wastewater using steam activated biomass soot and tire carbon black. J. Harzadous Mater. https://doi.org/10.1016/j.jhazmat.2018.09.061.

Arivoli, S., Hema, M., Martin, P., Prasath, D., 2009. Adsorption of malachite green onto carbon prepared from borassus bark. Arab. J. Sci. 31–36. https://doi.org/10.3390/catal11040504.

Arumugam, T.K., Krishnamoorthy, P., Rajagopalan, N.R., Nanthini, S., Vasudevan, D., 2019. Removal of malachite green from aqueous solutions using a modified chitosan composite. Int. J. Biol. Macromol. https://doi.org/10.1016/j.ijbiomac.2019.01.185.

Atunwa, B.T., Dada, A.O., Inyinbor, A.A., Pal, U., 2022. Synthesis, physiochemical and spectroscopic characterization of palm kernel shell activated carbon doped AgNPs (PKSAC@AgNPs) for adsorption of chloroquine pharmaceutical waste. Mater. Today Proc. https://doi.org/10.1016/j.matpr.2022.06.099.

Baek, M.-.H., Ijagbemi, C.O., Se-Jin, O., Kim, D.-S., 2010. Removal of Malachite Green from aqueous solution using degreased coffee bean. J. Harzadous Mater. 176, 820–828. https://doi.org/10.1016/j.jhazmat.2009.11.110.

Bai, X., Xu, M., Li, Q., Yu, L., 2022. Trajectory-battery integrated design and its application to orbital maneuvers with electric pump-fed engines. Adv. Sp. Res. 70, 825–841.

Bayode, A.A., Vieira, E.M., Moodley, R., Akpotu, S., De Camargo, A.S.S., Fatta-kassinos, D., Unuabonah, E.I., 2020a. Tuning ZnO/GO p-n heterostructure with carbon interlayer supported on clay for visible-light catalysis: removal of steroid estrogens in water. Chem. Eng. J. 3, 127668 https://doi.org/10.1016/j.cej.2020.127668.

Bayode, A.A., Agunbiade, F.O., Omorogie, M.O., Moodley, R., Olusola, B., Unuabonah Emmanue, O., 2020b. Clean technology for synchronous sequestration of charged organic micro-pollutant onto microwave-assisted hybrid clay materials. Environ. Sci. Pollut. Res. https://doi.org/10.1007/s11356-019-07563-z.

Bello, O.S., Oluwadamilola, E., Adesina, K., Adewale, S., Inyinbor, A.A., Dada, O.A., 2019a. Rhodamine B dye sequestration using Gmelina aborea leaf powder. Heliyon 5, e02872. https://doi.org/10.1016/j.heliyon.2019.e02872, 2872.

Bello, O.S., Adegoke, K.A., Sarumi, O.O., Lameed, O.S., 2019b. Functionalized locust bean pod (Parkia biglobosa) activated carbon for Rhodamine B dye removal. Heliyon 5, e02323. https://doi.org/10.1016/j.heliyon.2019.e02323.

Blanco-Flores, A., Toledo-Jaldin, H.P., Vilchis-Néstor, A.R., López-Téllez, G., Sánchez-Mendieta, V., Ávila-Márquez, D.M., 2020. Metallurgical slag properties as a support material for bimetallic nanoparticles and their use in the removal of malachite green dye. Adv. Powder Technol. 31, 2853–2865.

Chanzu, H.A., Onyari, J.M., Shiundu, P.M., 2012. Biosorption of malachite green from aqueous solutions onto polylactide/spent Brewery Grains films: kinetic and equilibrium studies. J. Polym. Environ. 20, 665–672. https://doi.org/10.1007/s10924-012-0479-5.

Choudhary, M., Kumar, R., Neogi, S., 2020. Activated biochar derived from Opuntia ficus-indica for the efficient adsorption of malachite green dye , Cu+2 and Ni+2 from water. J. Hazard Mater. 392, 122441 https://doi.org/10.1016/j.jhazmat.2020.122441.

Chowdhury, S., Mishra, R., Saha, P., Kushwaha, P., 2011. Adsorption thermodynamics , kinetics and isosteric heat of adsorption of malachite green onto chemically modi fi ed rice husk. DES 265, 159–168. https://doi.org/10.1016/j.desal.2010.07.047.

Conde-rivera, L.R., Suarez-escobar, A.F., Marin-perez, J.J., Junco-rodriguez, M.J., Lopez-suarez, F.E., 2021. TiO 2 supported on activated carbon from tire waste for ibuprofen removal. Mater. Lett. 291, 129590 https://doi.org/10.1016/j.matlet.2021.129590.

Cruz, G.J.F., Mondal, D., Rimaycuna, J., Soukup, K., Gómez, M.M., Solis, J.L., Lang, J., 2020. Agrowaste derived biochars impregnated with ZnO for removal of arsenic and lead in water. J. Environ. Chem. Eng. 8, 103800 https://doi.org/10.1016/j.jece.2020.103800.

Cui, Y., Su, W., Xing, Y., Hao, L., Sun, Y., Cai, Y., 2023. Experimental and simulation evaluation of CO2/CO separation under different component ratios in blast furnace gas on zeolites. Chem. Eng. J. 472, 144579.

Dada, O.A., Adekola, F.A., Odebunm, E.O., Dada, F.E., Bello, O.S., Ogunlaja, A.S., 2020a. Bottom-up approach synthesis of core-shell nanoscale zerovalent iron (CS-nZVI): physicochemical and spectroscopic characterization with Cu(II) ions adsorption application. MethodsX 7, 100976. https://doi.org/10.1016/j.mex.2020.100976.

Dada, A.O., Adekola, F.A., Odebunmi, E.O., 2017(a). Liquid phase scavenging of Cd (II) and Cu (II) ions onto novel nanoscale zerovalent manganese (nZVMn): equilibrium, kinetic and thermodynamic studies. Environ. Nanotechnology, Monit. Manag. 8, 63–72. https://doi.org/10.1016/j.enmm.2017.05.001.

Dada, A.O., Adekola, F.A., Odebunmi, E.O., 2017(b). A novel zerovalent manganese for removal of copper ions: synthesis, characterization and adsorption studies. Appl. Water Sci. 7, 1409–1427. https://doi.org/10.1007/s13201-015-0360-5.

Dada, A.O., Adekola, F.A., Odebunmi, E.O., Dada, F.E., Bello, O.M., Akinyemi, B.A., Bello, O.S., Umukoro, O.G., 2020b. Sustainable and low-cost Ocimum gratissimum for biosorption of indigo carmine dye: kinetics, isotherm, and thermodynamic studies. Int. J. Phytoremediation 0, 1–14. https://doi.org/10.1080/15226514.2020.1785389.

Dada, A.O., Inyinbor, A.A., Bello, O.S., Tokula, B.E., 2021. Novel plantain peel activated carbon–supported zinc oxide nanocomposites (PPAC-ZnO-NC) for adsorption of chloroquine synthetic pharmaceutical used for COVID-19 treatment. Biomass Convers. Biorefinery 1, 3. https://doi.org/10.1007/s13399-021-01828-9.

Dada, A.O., Inyinbor, A.A., Tokula, B.E., Bello, O.S., Pal, U., 2022. Preparation and characterization of rice husk activated carbon-supported zinc oxide nanocomposite (RHAC-ZnO-NC). Heliyon 8, e10167. https://doi.org/10.1016/j.heliyon.2022.e10167.

Dada, A.O., Adediran, G.O., Fehintoluwa, E.D., Charity, O.A., Adewumi, O.D., Ojediran, J., Tokula, B.E., Olusanya, S.O., 2023. Isotherm and statistical validity modelings of adsorption of endocrine disruptive Cr(VI) onto calcinated earthworm cast, 2023. Int. Conf. Sci. Eng. Bus. Sustain. Dev. Goals (SEB-SDG), Omu-Aran, Niger 1–7. https://doi.org/10.1109/SEB-SDG57117.2023.10124501.

Deb, A., Kanmani, M., Debnath, A., Bhowmik, K.L., Saha, B., 2019. Ultrasonic assisted enhanced adsorption of methyl orange dye onto polyaniline impregnated zinc oxide nanoparticles: kinetic, isotherm and optimization of process parameters. Ultrason. Sonochem. 54, 290–301. https://doi.org/10.1016/j.ultsonch.2019.01.028.

Dehbi, A., Dehmani, Y., Omari, H., Lammini, A., Elazhari, K., Abouarnadasse, S., Abdallaoui, A., 2020. Comparative study of malachite green and phenol adsorption on synthetic hematite iron oxide nanoparticles (α-Fe2O3). Surface. Interfac. 21, 340–366. https://doi.org/10.1016/j.jhazmat.2016.08.072.

Ding, C., Cheng, W., Sun, Y., Wang, X., 2015. Effects of Bacillus subtilis on the reduction of U(VI) by nano-Fe0. Geochim. Cosmochim. Acta 165, 86–107. https://doi.org/10.1016/j.gca.2015.05.036.

Ekpete, O.A., Marcus, A.C., Osi, V., 2017. Preparation and characterization of activated carbon obtained from plantain (musa paradisiaca) fruit stem. Hindawi J. Chem. 2017 https://doi.org/10.1155/2017/8635615.

El-Naggar, N.E.A., Hussein, M.H., Shaaban-Dessuuki, S.A., Dalal, S.R., 2020. Production, extraction and characterization of Chlorella vulgaris soluble polysaccharides and their applications in AgNPs biosynthesis and biostimulation of plant growth. Sci. Rep. 10, 1–19. https://doi.org/10.1038/s41598-020-59945-w.

Elwardany, R.E., Shokry, H., Mustafa, A.A., Ali, A.E., 2023. Influence of the prepared activated carbon on cellulose acetate for malachite green dye removal from aqueous solution. Macromol. Res. 31, 1043–1060. https://doi.org/10.1007/s13233-023-00187-w.

Feng, X., Zhu, J., Song, K., Zeng, J., Zhou, X., Guo, X., Lin, K., Zhang, C., Xie, C., Shi, J.-W., 2024. Insight into the reasons for enhanced NH3-SCR activity and SO2 tolerance of Mn-Co layered oxides. Sep. Purif. Technol. 336, 126285.

Firdaus, M., Yusop, M., Abdullah, A.Z., Ahmad, M.A., 2023. Malachite green dye adsorption by jackfruit based activated carbon: optimization, mass transfer simulation and surface area prediction. Diam. Relat. Mater. 136, 109991 https://doi.org/10.1016/j.diamond.2023.109991.

Foo, K.Y., Hameed, B.H., 2010. Insights into the modeling of adsorption isotherm systems. Chem. Eng. J. 156, 2–10. https://doi.org/10.1016/j.cej.2009.09.013.

Gan, H.Y., Leow, L.-E., Ong, S.-T., 2017. Utilization of corn cob and TiO2 photocatalyst thin films for dyes removal. Acta Chim. Slov. 64, 144–158. https://doi.org/10.17344/acsi.2016.2983.

Giri, B.S., Sonwani, K.R., Varjani, S., Chaurasia, D., Varadavenkatesan, T., Chaturvedi, P., Yadav, S., Katiyar, V., Singh, R.S., Pandey, A., 2022. Highly efficient bio-adsorption of Malachite green using Chinese Fan-Palm Biochar (Livistona chinensis). Chemosphere 287, 132282. https://doi.org/10.1016/j.chemosphere.2021.132282.

Guechi, E.K., Hamdaoui, O., 2016. Sorption of malachite green from aqueous solution by potato peel: kinetics and equilibrium modeling using non-linear analysis method. Arab. J. Chem. 9, S416–S424. https://doi.org/10.1016/j.arabjc.2011.05.011.

Gündüz, F., Bayrak, B., 2017. Biosorption of malachite green from an aqueous solution using pomegranate peel: equilibrium modelling, kinetic and thermodynamic studies. J. Mol. Liq. 243, 790–798. https://doi.org/10.1016/j.molliq.2017.08.095.

Guo, D., Li, H., Xu, Z., Nie, Y., 2023. Development of pyrene-based MOFs probe for water content and investigations on their mechanochromism and acidochromism. J. Alloys Compd. 968, 172004.

Gupta, N., Kushwaha, A.K., Chattopadhyaya, M.C., 2016. Application of potato (Solanum tuberosum) plant wastes for the removal of methylene blue and malachite green dye from aqueous solution. Arab. J. Chem. 9, S707–S716. https://doi.org/10.1016/j.arabjc.2011.07.021.

He, H., Shi, J., Yu, S., Yang, J., Xu, K., He, C., Li, X., 2024. Exploring green and efficient zero-dimensional carbon-based inhibitors for carbon steel: from performance to mechanism. Constr. Build. Mater. 411, 134334.

Hemmati, F., Norouzbeigi, R., Sarbisheh, F., Shayesteh, H., 2016. Malachite green removal using modified sphagnum peat moss as a low-cost biosorbent: kinetic, equilibrium and thermodynamic studies. J. Taiwan Inst. Chem. Eng. 58, 482–489.

Hock, P.E., Nurfaiz, A., Faizal, M., Sirajo, L., Abbas, M., Zaini, A., 2023. Insight into kinetics , equilibrium , and thermodynamics of malachite green adsorption onto banana peel adsorbents. Biomass Convers. Biorefinery. https://doi.org/10.1007/s13399-023-04117-9.

Inyinbor, A.A., Adekola, F.A., Olatunji, G.A., 2016. Kinetics , isotherms and thermodynamic modeling of liquid phase adsorption of Rhodamine B dye onto Raphia hookerie fruit epicarp. Water Resour. Ind. 15, 14–27. https://doi.org/10.1016/j.wri.2016.06.001.

Kuang, W., Wang, H., Li, X., Zhang, J., Zhou, Q., Zhao, Y., 2018. Application of the thermodynamic extremal principle to diffusion-controlled phase transformations in Fe-CX alloys: modeling and applications. Acta Mater. 159, 16–30.

Kumar, M., Sarsaiya, S., Patel, A., Juneja, A., Duan, Y., Pandey, A., Zhang, Z., Taherzadeh, M.J., 2020. Refining biomass residues for sustainable energy and bio-products : an assessment of technology , its importance , and strategic applications in circular bio-economy. Renew. Sustain. Energy Rev. 127, 109876 https://doi.org/10.1016/j.rser.2020.109876.

Lari, L., Steinhauer, S., Lazarov, V.K., 2020. In situ TEM oxidation study of Fe thin-film transformation to single-crystal magnetite nanoparticles. J. Mater. Sci. 55, 12897–12905. https://doi.org/10.1007/s10853-020-04917-8.

Lazim, Z.M., Hadibarata, T., Yusop, Z., Nazifa, T.H., Abdullah, N.H., Nuid, M., 2021. Bisphenol A removal by adsorption using waste biomass : isotherm and kinetic studies. Biointerface Res. Appl. Chem. 11, 8467–8481.

Li, H., Xu, X., Liu, Y., Hao, Y., Xu, Z., 2023. Fluorophore molecule loaded in Tb-MOF for dual-channel fluorescence chemosensor for consecutive visual detection of bacterial spores and dichromate anion. J. Alloys Compd. 944, 169138.

Liu, G., Abukhadra, M.R., El-sherbeeny, A.M., Mostafa, A.M., Elmeligy, M.A., 2020. Insight into the photocatalytic properties of diatomite@Ni/NiO composite for effective photo-degradation of malachite green dye and photo-reduction of Cr (VI) under visible light. J. Environ. Manage. 254, 109799 https://doi.org/10.1016/j.jenvman.2019.109799.

Masoudian, N., Rajabi, M., Ghaedi, M., 2019. Titanium oxide nanoparticles loaded onto activated carbon prepared from bio-waste watermelon rind for the efficient ultrasonic-assisted adsorption of Congo red and phenol red dyes from wastewaters. Polyhedron 173, 114105. https://doi.org/10.1016/j.poly.2019.114105.

Merrad, S., Abbas, M., Trari, M., 2023. Adsorption of malachite green onto walnut shells : kinetics , thermodynamic , and regeneration of the adsorbent by chemical process. Fibers Polym. 24, 1067–1081. https://doi.org/10.1007/s12221-023-00025-x.

Mittal, A., 2006. Adsorption kinetics of removal of a toxic dye, malachite green, from wastewater by using hen feathers. J. Hazard Mater. 133, 196–202. https://doi.org/10.1016/j.jhazmat.2005.10.0176326001.

Mosebolatan, J., Ayorinde, M., Adelaja, Y., 2023. Valorization of microwave-assisted H3PO4-activated plantain (Musa paradisiacal L) leaf biochar for malachite green sequestration : models and mechanism of adsorption. Results Eng 18, 101129. https://doi.org/10.1016/j.rineng.2023.101129.

Mudyawabikwa, B., Mungondori, H.H., Tichagwa, L., Katwire, D.M., 2017. Methylene blue removal using a low-cost activated carbon adsorbent from tobacco stems: kinetic and equilibrium studies. Water Sci. Technol. 75, 2390–2402. https://doi.org/10.2166/wst.2017.041.

Muinde, V.M., Onyari, J.M., Wamalwa, B., Wabomba, J.N., 2020. Adsorption of malachite green dye from aqueous solutions using mesoporous chitosan–zinc oxide composite material. Environ. Chem. Ecotoxicol. 2, 115–125. https://doi.org/10.1016/j.ijhydene.2019.03.149.

Naseeruteen, F., Hamid, N.S.A., Suah, F.B.M., Ngah, W.S.W., Mehamod, F.S., 2018. Adsorption of malachite green from aqueous solution by using novel chitosan ionic liquid beads. Int. J. Biol. Macromol. 107, 1270–1277. https://doi.org/10.1016/j.ijbiomac.2017.09.111.

Obayomi, K.S., Lau, S.Y., Danquah, M.K., Zhang, J., Chiong, T., Meunier, L., Gray, S.R., Rahman, M.M., 2023a. Green synthesis of graphene-oxide based nanocomposites for efficient removal of methylene blue dye from wastewater. Desalination, 116749.

Obayomi, K.S., Lau, S.Y., Ibrahim, O., Zhang, J., Meunier, L., Aniobi, M.M., Atunwa, B.T., Pramanik, B.K., Rahman, M.M., 2023b. Removal of Congo red dye from aqueous environment by zinc terephthalate metal organic framework decorated on silver nanoparticles-loaded biochar: mechanistic insights of adsorption. Microporous Mesoporous Mater. 355, 112568.

Obayomi, K.S., Lau, S.Y., Danquah, M.K., Zhang, J., Chiong, T., Meunier, L., Rahman, M.M., 2023c. Selective adsorption of organic dyes from aqueous environment using fermented maize extract-enhanced graphene oxide-durian shell derived activated carbon composite. Chemosphere 339, 139742.

Ojediran, J.O., Dada, A.O., Aniyi, S.O., David, R.O., 2020. Functionalized Zea Mays Cob (FZMC) as low-cost agrowaste for effective adsorption of malachite green dyes data set. Chem. Data Collect. 30, 100563 https://doi.org/10.1016/j.cdc.2020.100563.

Ojediran, J.O., Dada, A.O., Aniyi, S.O., David, R.O., Adewumi, A.D., 2021. Mechanism and isotherm modeling of effective adsorption of malachite green as endocrine

disruptive dye using Acid Functionalized Maize Cob (AFMC). Sci. Rep. 11, 1–15. https://doi.org/10.1038/s41598-021-00993-1.
Quesada, H.B., Cusioli, L.F., de O Bezerra, C., Baptista, A.T.A., Nishi, L., Gomes, R.G., Bergamasco, R., 2019. Acetaminophen adsorption using a low-cost adsorbent prepared from modified residues of Moringa oleifera Lam. seed husks. J. Chem. Technol. Biotechnol. 94, 3147–3157. https://doi.org/10.1002/jctb.6121.
Rangabhashiyam, S., Balasubramanian, P., 2018. Performance of novel biosorbents prepared using native and NaOH treated Peltophorum pterocarpum fruit shells for the removal of malachite green. Bioresour. Technol. 9, 75–81.
Rangabhashiyam, S., Lata, S., Balasubramanian, P., 2018. Biosorption characteristics of methylene blue and malachite green from simulated wastewater onto Carica papaya wood biosorbent. Surface. Interfac. 10, 197–215. https://doi.org/10.1016/j.cap.2020.04.006.
Saha, P., Chowdhury, S., Gupta, S., Kumar, I., Kumar, R., 2010a. Assessment on the removal of malachite green using tamarind fruit shell as biosorbent. Clean 38, 437–445. https://doi.org/10.1002/clen.200900234.
Saha, P., Chowdhury, S., Gupta, S., Kumar, I., 2010b. Insight into adsorption equilibrium, kinetics and thermodynamics of Malachite Green onto clayey soil of Indian origin. Chem. Eng. J. 165, 874–882. https://doi.org/10.1016/j.cej.2010.10.048.
Saleh, T.A., Tuzen, M., Sarı, A., 2017. Magnetic activated carbon loaded with tungsten oxide nanoparticles for aluminum removal from waters Highlights. J. Environ. Chem. Eng. 5, 2853–2860. https://doi.org/10.1016/j.jece.2017.05.038.
Santhi, T., Manonmani, S., Vasantha, V.S., Chang, Y.T., 2011. A new alternative adsorbent for the removal of cationic dyes from aqueous solution. Arab. J. Chem. https://doi.org/10.1016/j.arabjc.2011.06.004.
Santhosh, K., Sk, S., Chouti, S., Gonuguntla, S., Ega, S.P., Tiwari, A., Pal, U., 2021. Tailoring hierarchical porous TiO2 based ternary rGO/NiO/TiO2 photocatalyst for efficient hydrogen production and degradation of Rhodamine B. J. Mol. Struct. 1235, 130222 https://doi.org/10.1016/j.molstruc.2021.130222.
Sartape, A.S., Mandhare, A.M., Jadhav, V.V., Raut, P.D., Anuse, M.A., Kolekar, S.S., 2017. Removal of malachite green dye from aqueous solution with adsorption technique using Limonia acidissima (wood apple) shell as low cost adsorbent. Arab. J. Chem. 10, S3229–S3238. https://doi.org/10.1016/j.arabjc.2013.12.019.
Selvasembian, R., Balasubramanian, B., 2018. Utilization of Unconventional Lignocellulosic Waste Biomass for the Biosorption of Toxic Triphenylmethane Dye Malachite Green from Aqueous Solution. Korean Physical Society. https://doi.org/10.1080/15226514.2017.1413329.
Shayesteh, H., Rahbar-Kelishami, A., Norouzbeigi, R., 2016. Adsorption of malachite green and crystal violet cationic dyes from aqueous solution using pumice stone as a low-cost adsorbent: kinetic, equilibrium, and thermodynamic studies. Desalin. Water Treat. 57, 12822–12831.
Somsiripan, T., Sangwichien, C., 2023. Enhancement of adsorption capacity of Methylene blue , Malachite green, and Rhodamine B onto KOH activated carbon derived from oil palm empty fruit bunches. Arab. J. Chem. 16, 105270 https://doi.org/10.1016/j.arabjc.2023.105270.
Sridhar, R., Ramanane, U.U., Rajasimman, M., 2018. ZnO nanoparticles – synthesis, characterization and its application for phenol removal from synthetic and pharmaceutical industry wastewater. Environ. Nanotechnology, Monit. Manag. 10, 388–393. https://doi.org/10.1016/j.enmm.2018.09.003.
Sudhakar, P., Soni, H., 2018. Efficient removal of organic pollutants with activated carbon derived from palm shell: spectroscopic characterization and experimental optimization. Biochem. Pharmacol. S2213–S3437. https://doi.org/10.1016/j.jece.2018.04.013.
Sudhakar, P., Mall, I.D., Srivastava, V.C., 2015. Adsorptive removal of bisphenol-A by rice husk ash and granular activated carbon — a comparative study. Desalin. Water Treat. 37–41. https://doi.org/10.1080/19443994.2015.1050700.
Taha, M.H.M., 2023. Optimization study of the adsorption of malachite green removal by MgO nano- composite, nano-bentonite and fungal immobilization on active carbon using response surface methodology and kinetic study. Environ. Sci. Eur. 1–37. https://doi.org/10.1186/s12302-023-00728-1.
Thi, L., Thuy, T., Thuy, P.T., Thi, P., Anh, G., Tien, N.A., 2023. Simultaneous adsorption of malachite green , methyl orange, and rhodamine B with TiO2/macadamia nutshells-derived activated carbon composite Simultaneous adsorption of malachite green , methyl orange , and rhodamine B with TiO2/macadamia nutshells-derived. Mater. Res. Express 10.
Tokula, B.E., Dada, A.O., Inyinbor, A.A., Aremu, C.O., Obayomi, K.S., Adewumi, O.D., Adekola, F.A., Ojediran, J., 2023a. Preparation, physicochemical and spectroscopic characterization of low-cost acid functionalised rice husk activated carbon (AF-RHAC). In: Int. Conf. Sci. Eng. Bus. Sustain. Dev. Goals Omu-Aran, Niger, pp. 1–6. https://doi.org/10.1109/SEB-SDG57117.2023.10124611, 2023.
Tokula, B.E., Dada, A.O., Inyinbor, A.A., Obayomi, K.S., Bello, O.S., Pal, U., 2023b. Agro-waste based adsorbents as sustainable materials for effective adsorption of Bisphenol A from the environment : a review. J. Clean. Prod. 388, 135819 https://doi.org/10.1016/j.jclepro.2022.135819.
Wang, M., Li, G., Huang, L., Xue, J., Liu, Q., Bao, N., Huang, J., 2017. Study of ciprofloxacin adsorption and regeneration of activated carbon prepared from Enteromorpha prolifera impregnated with H3PO4 and sodium benzenesulfonate. Ecotoxicol. Environ. Saf. 139, 36–42. https://doi.org/10.1016/j.ecoenv.2017.01.006.
Wang, F., Zeng, Q., Su, W., Zhang, M., Hou, L., Wang, Z., 2019. Adsorption of bisphenol A on peanut shell biochars: the effects of surfactants. Hindawi J. Chem. 2019, 10. https://doi.org/10.1155/2019/2428505.
Wang, Z., Fernández-Blanco, C., Chen, J., Veiga, M.C., Kennes, C., 2024a. Effect of electron acceptors on product selectivity and carbon flux in carbon chain elongation with Megasphaera hexanoica. Sci. Total Environ. 912, 169509.
Wang, N., Li, X., Lian, X., Zhuang, Q., Wang, J., Li, J., Qian, H., Miao, K., Wang, Y., Luo, X., 2024b. Others, acetate ions facilitated immobilization of highly dispersed transition metal oxide nanoclusters in mesoporous silica. Inorg. Chem. 63 (9), 4393–4403. https://doi.org/10.1021/acs.inorgchem.4c00024.
Workie, E., Mengist, Y., Sisay, M., Ma, A., 2019. Preparation , characterization and cost analysis of activated biochar and hydrochar derived from agricultural waste : a comparative study. SN Appl. Sci. 1, 1–8. https://doi.org/10.1007/s42452-019-0936-z.
Xu, P., Liu, X., Zhao, Y., Lan, D., Shin, I., 2023. Study of graphdiyne biomimetic nanomaterials as fluorescent sensors of ciprofloxacin hydrochloride in water environment. Desalin Water Treat 302, 129–137.
Xue, Y., Liu, X., Zhang, N., Shao, Y., Xu, C.C., 2023. Enhanced photocatalytic performance of iron oxides@ HTCC fabricated from zinc extraction tailings for methylene blue degradation: investigation of the photocatalytic mechanism. Int. J. Miner. Metall. Mater. 30, 2364–2374.
Y, V., H, A., N, P., Sreedhar, I., A, S.S., 2022. Enhanced photocatalytic activity of TiO2–NiO heterojunctions supported on alumina for malachite green degradation. Int. J. Environ. Sci. Technol. https://doi.org/10.1007/s13762-022-04038-6.
Yildirim, A., Acay, H., 2020. Biosorption studies of mushrooms for two typical dyes. J. Turk. Chem. Soc. OTCSA., J. Turkish Chem. Soc. OTCSA 1, 95–306. https://doi.org/10.18596/jotcsa.581007.
Zeng, Y., Xue, Y., 2019. Novel crayfish shell biochar nanocomposites loaded with Ag-TiO2 nanoparticles exhibit robust antibacterial activity. Water. Air. Soil Pollut. 230, 50.
Zheng, Y., Liu, Y., Guo, X., Chen, Z., Zhang, W., Wang, Y., Tang, X., Zhang, Y., Zhao, Y., 2020. Sulfur-doped g-C3N4/rGO porous nanosheets for highly efficient photocatalytic degradation of refractory contaminants. J. Mater. Sci. \& Technol. 41, 117–126.
Dada, A.O., Sagar, V., Yendrapati, T.P.,Abraham, B.M., Vijayanand, P., Ujjwal, P.2023. Biosynthetic modulation of carbon-doped ZnO for rapid photocatalytic endocrine disruptive remediation and hydrogen evolution. J. Clean. Prod. 394,136393. doi: 10.1016/j.jclepro.2023.136393.